PARTIAL VOLUME EFFECT (PVE) CORRECTION IN NUCLEAR IMAGING: SPECIAL PHANTOM DEVELOPMENT AND VALIDATION IN CLINICAL DEVICES

by

Güneş Yavuz

B.S., in Statistics, Middle East Technical University, 1989

M.S., in Biomedical Engineering, Boğaziçi University, 2000

M.B.A. in Marketing Management, Yeditepe University, 2018

Submitted to the Institute of Biomedical Engineering

in partial fulfillment of the requirements

for the degree of

Doctor

of

Philosophy

Boğaziçi University

2024

PARTIAL VOLUME EFFECT (PVE) CORRECTION IN NUCLEAR IMAGING: SPECIAL PHANTOM DEVELOPMENT AND VALIDATION IN CLINICAL DEVICES

APPROVED BY:

Prof. Dr. Cengizhan Öztürk ..... (Thesis Advisor)

Prof. Dr. Tevfik Fikret Çermik .....

Prof. Dr. Esin Öztürk Işık .....

Prof. Dr. Can Yücesoy .....

Prof. Dr. Nalan Alan .....

DATE OF APPROVAL: 15 August 2024

ACKNOWLEDGMENTS

I would like to thank all people who have helped and inspired me during my doctoral study.

I especially want to thank my advisor, Prof. Dr. Cengizhan Öztürk, for his guidance throughout my protracted research studies at Boğaziçi University. His perpetual energy in research and technology had motivated all his advisees including me. He provides me constant encouragement and a perfect balance between guidance and freedom throughout this study. I would like to thank to my Mentor Prof. Dr. Tevfik Fikret Çermik for his trust and support during years in my study. He is the one who has encourged me to study on Partial Volume Effect (PVE) correction in PET Imaging. I thank to my friend Dr. Bilal Kovan for his continous support and guideness during my study. I thank to Prof. Dr. Seyhan Karaçavuş who has believed me and encourged me in this study. I also thank to Prof. Dr. Abbas Alavi and Prof. Dr. Habib Zahidi for their personal inspirations and friendship.

I was delighted to be a part of Turkish Nuclear Medicine Society. Special thanks to Prof. Dr. Serkan Kuyumcu from İstanbul University- Istanbul Medical Faculty Nuclear Medicine (NM) Department, Prof. Dr. Tevfik Fikret Çermik and Dr. Ömer Şahin for all his support in image processing and analyzing from Istanbul Training and Research Hospital NM Department, Prof. Dr. Tamer Atasever and Dr. Tansel Çakır from Medipol Mega Hospital NM Dept, and Prof. Dr. Tamer Özülker from Dr. Cemil Taşçıoğlu Training and Research Hospital. They all supported me to do clinical studies in their hospitals. I also would like to thank to Ahmet Turan Atalay who was the key person for the phantom related in house work at the Boğaziçi University, thanks to his Asistant Adem Yiğitaslan as well. Last but not least, Prof. Dr. Nalan Alan Selçuk and Dr. Türkay Toklu from Yeditepe University where I did all post-processing parts of this study. Of course, special thanks to my buddy Dr. Can Özcan and thanks to all my friends who are the part of this long journey.

Financial support for my study comes partially from the Boğaziçi University Scientific Research Projects Fund (BAP Project code - 19944), which is greatly appreciated.

My deepest gratitude goes to my family for their unflagging love and support throughout my life; tthis thesis simply would have been impossible without them. Thanks to my late father Hakkı Yavuz for his guidance and visions that he shared with me throughout his short life. I have always been honored to be his daughter. I am grateful to my late mother Ferhan Yavuz for her love, kindness and support in my life. She was always my role model with her unlimited patience, confidence, love and eagerness. I always feel proud with my siblings. I am proud of my brother Prof. Dr. Hasan Ulaş Yavuz and my sister Attorney Lale Işıl Yavuz Bozatlı for their talents and success in their lives. I also thank to my brother in law Dr. Ali Nahit Bozatlı and sister in law Prof. Dr. Dudu Özkum Yavuz for their kindness and support. I hope that they will be very healthy and happy with their families in their long lives. Last but certainly not least, I would like to express my heartfelt gratitude to my beloved nephews, Ali Yavuz and Ahmet Aral, and my little niece, Hazar İz. Your love, smiles, and endless joy have been a constant source of happiness and motivation throughout this journey. Thank you for bringing so much light into my life.

This thesis is dedicated to the memory of my dear mother Ferhan YAVUZ, and my dear father Hakkı YAVUZ.

ACADEMIC ETHICS AND INTEGRITY STATEMENT

I, Güneş Yavuz, hereby certify that I am aware of the Academic Ethics and Integrity Policy issued by the Council of Higher Education (YÖK) and I fully acknowledge all the consequences due to its violation by plagiarism or any other way.

Name :

Signature:

Date:

ABSTRACT

PARTIAL VOLUME EFFECT (PVE) CORRECTION IN NUCLEAR IMAGING: SPECIAL PHANTOM DEVELOPMENT AND VALIDATION IN CLINICAL DEVICES

Positron Emission Tomography (PET) imaging is a powerful and widely utilized modality in the field of Nuclear Medicine, particularly for the diagnosis and monitoring of cancer. This project aims to design and produce a unique anthropomorphic PET phantom that mimics human tissue properties; Utilize the developed phantom to calculate corrected Standard Uptake Values (SUVs) for oncological lesions by applying Recovery Coefficients (RCs) determined for Partial Volume Effect (PVE) correction. SUV is a widely utilized quantitative parameter in PET imaging, representing the concentration of radiotracer uptake within a region of interest (ROI) relative to its overall distribution in the body. However, the accuracy of SUV measurements can be compromised by the PVE, a phenomenon that arises when the spatial resolution of the imaging system is insufficient to clearly distinguish between adjacent tissues or structures within a single voxel, leading to underestimation or overestimation of radiotracer concentration. This dissertation is dedicated to exploring the critical area of PVE correction in F18-FDG PET imaging, focusing on the use of anthropomorphic phantoms as a fundamental platform for in-depth studies. By simulating anatomical conditions representative of the human body, anthropomorphic phantoms serve as important test phantoms for the evaluation of correction algorithms and provide insights into their efficacy and limitations. Through methodical experimentation and careful analysis, the research described here aims to make a significant contribution towards the refinement of PVE correction strategies, to increase the accuracy and reliability of F18- FDG PET imaging in the future.

Keywords: PET-CT, FDG-PET, Partial Volume Effect (PVE), PVE Correction (PVEC), Anthropomorphic Phantom, Recovery Coefficients, SUV.

ÖZET

NÜKLEER GÖRÜNTÜLEMEDE PARSİYEL HACİM ETKİSİ (PVE) DÜZELTMESİ: ÖZEL FANTOM GELİŞTİRİLMESİ VE KLİNİK CİHAZLARDA DOĞRULANMASI

Pozitron Emisyon Tomografisi (PET) görüntüleme, özellikle kanserin tanı ve takibinde olmak üzere, Nükleer Tıp alanında güçlü ve yaygın olarak kullanılan bir modalitedir. Bu proje ile insan doku özelliklerini taklit eden özgün bir antropomorfik PET fantomu tasarlamak ve üretmek; ve geliştirilen fantomu kullanarak, Parsiyel Hacim Etkisi (PVE) düzeltmesi için belirlenen Kurtarma Katsayıları (RC) uygulanmak suretiyle, onkolojik lezyonlar için düzeltilmiş Standart Tutulum Değeri (SUV) hesaplamalarını gerçekleştirmek amaçlanmıştır. SUV, PET görüntülemede yaygın olarak kullanılan bir niceliksel parametredir ve bir ilgi bölgesindeki (ROI) radyoizotop tutulum yoğunluğunun, vücutta genel dağılıma oranını temsil eder. Ancak, SUV ölçümlerinin doğruluğu, Görüntüleme sisteminin uzaysal çözünürlüğü, tek bir vokseldeki komşu dokular veya yapılar arasında net bir ayrım yapamayacak kadar yetersiz olduğunda, yani PVE olarak adlandırılan bir fenomenin ortaya çıkmasıyla bozulabilir. Bu durum, radyoizotop yoğunluğunun olduğundan düşük veya yüksek değerlendirilmesine yol açabilir. Bu tez, F18-FDG PET görüntülemesinde PVE düzeltmesinin kritik bir alt alanına adanmış olup, antropomorfik fantomların derinlemesine çalışmalar için temel bir platform olarak kullanımına odaklanmaktadır. İnsan vücudunu temsil eden anatomik koşulları simüle eden antropomorfik fantomlar; düzeltme algoritmalarının değerlendirilmesi için önemli bir test ortamı sağlar ve etkinlikleri ile sınırlamalarına dair öngörü sunar. Bu tez çalışması ile; metodik bir yaklaşım ve dikkatli analizler ile, daha doğru PVE düzeltme stratejilerinin geliştirilmesine bir katkıda bulunmak ve bu yolla da F18-FDG PET görüntülemelerinin doğruluğunu ve güvenilirliğini artırmak amaçlanmıştır.

Anahtar Sözcükler: PET-BT, FDG-PET, Parsiyel Hacim Etkisi (PVE), PVE Düzeltmesi (PVEC), Antropomorfik Fantom, Kurtarma Katsayıları, SUV.

TABLE OF CONTENTS

ACKNOWLEDGMENTS . . . iii
ACADEMIC ETHICS AND INTEGRITY STATEMENT . . . vi
ABSTRACT . . . vii
ÖZET . . . viii
LIST OF FIGURES . . . xii
LIST OF TABLES . . . xv
LIST OF SYMBOLS . . . xvi
LIST OF ABBREVIATIONS . . . xvii
1. INTRODUCTION . . . 1
2. NUCLEAR PHYSICS . . . 3
2.1 Nuclear Medican Physics and Radiation . . . 4
2.1.1 Definition and Types of Radiation . . . 4
2.1.2 Radiation Sources . . . 5
2.1.3 Types of Radioactive Decay . . . 5
2.2 Radiation Does Units . . . 12
2.2.1 Activity Unit (Curie and Becquerel) . . . 12
2.2.2 Irradiation Unit . . . 13
2.2.3 Absorbed Dose Unit . . . 14
2.2.4 Equivalent Does Unit . . . 14
2.3 Fundamental Rules of Radiation Protection . . . 15
2.3.1 Protection Methods Against Radiation . . . 15
3. BASICS OF PET AND PET-CT IMAGING . . . 17
3.1 History of Positron Emission Tomography (PET) . . . 17
3.2 Basic of PET Physics . . . 18
3.2.1 Specifications of PET and PET-CT Scanner . . . 19
3.2.2 Attenuation Correction . . . 21
3.2.3 PET-CT Technology . . . 23
3.2.4 SUV - Standard Uptake Volume and Digitization . . . 30
3.2.5 Partial Volume Effect (PVE) . . . 32

3.2.6 Partial Volume Effect Correction (PVEC) 33
3.3 PET Calibration and Phantoms 36
3.3.1 Standardization and SUV 36
3.3.2 Calibration Phantoms 37
3.3.3 Phantom Studies 37
3.3.4 Cross Calibration 45
3.3.5 National Electrical Manufacturers Association (NEMA) Standards 46
3.3.6 Quality Control 46
4. MATERIAL AND METHODOLOGY 47
4.1 Introduction 47
4.2 Design, modification and production of an anthropomorphic phantom for PVE correction 50
4.3 Design and production of Cylinders and Spheres with 3D Printer Technology 54
4.3.1 2-D Raw drawings of Spheres in Solidworks program 55
4.3.2 3-D Printing of Spheres 56
4.3.3 3-D Raw Drawings and printing of cylinders 60
4.4 PET-CT System 62
4.4.1 Analog PET-CT System 63
4.4.2 Digital PET-CT System 63
4.5 Hot Lab and Equipments 63
4.6 FDG preperation and injection 64
4.7 Anthropomorphic Phantom Scans in Clinical Sites and Hospitals 65
4.7.1 Istanbul University, Istanbul Medical Faculty, NM Department - GE PET-CT System specifications 65
4.7.2 Health Sciences University, Istanbul Training and Research Hospital, Nuclear Medicine Clinic - Siemens PET-CT System specificatons 67
4.7.3 Medipol University, Mega Hospital, Nuclear Medicine Department - Philips PET-CT System specificatons 70

4.7.4 Prof. Dr. Cemil Taşçıoğlu City Hospital, Health Application and Research Center, Nuclear Medicine Clinic - GE Digital PET-CT System specificatons 72
4.8 Scan parameters and injected radioactivity dose (FDG) to spheres and to cylinders for Back Ground (BG) activities 75
4.9 Image acqusition, reconstruction and quantification 77
5. RESULTS 80
6. DISCUSSION 85
7. CONCLUSION 92
8. FUTURE DIRECTIONS IN PET IMAGING 94
REFERENCES 95

LIST OF FIGURES

Figure 2.1	Structure of (a) glucose; (b) 2 DG and (c) F-18 FDG.	10
Figure 3.1	Formation of annihilation photons.	19
Figure 3.2	Attenuation effect: (a) deeper-more attenuation; (b) brighter-less attenuation.	22
Figure 3.3	Illustration of positron annihilation.	24
Figure 3.4	Types of coincidence events detected in PET imaging.	25
Figure 3.5	Transaxial PET images of a phantom uniformly filled with Fluorine-18 solution.	27
Figure 3.6	PET-NEMA/EIC body phantom spheres in 10, 13, 17, 22, 28, and 37 mm sizes.	38
Figure 3.7	PET-NEMA body phantom.	39
Figure 3.8	Phases of the phantom production.	40
Figure 3.9	Positioning of the PET-NEMA phantom in a PET scan.	41
Figure 3.10	CIRS ATOM dosimetry phantoms.	42
Figure 3.11	Pediatric anthropomorphic training phantoms.	44
Figure 3.12	Alderson anthropomorphic radiation therapy phantom.	45
Figure 4.1	Re-designed and modified anthropomorphic body phantom.	50
Figure 4.2	Human-like vertebra phantom	51
Figure 4.3	Solidworks of 2D raw drawings of anthropomorphic body phantom.	52
Figure 4.4	(a) Human skeleton; (b) The adult human model.	52
Figure 4.5	Anthropomorphic body phantom Arpat and the hole for the plexiglass spheres placement.	54
Figure 4.6	The solid models of the spheres.	55
Figure 4.7	“Vero black” out of 3D printer resin pallette.	56
Figure 4.8	The first vero black - resin 3D printed prototypes.	57
Figure 4.9	Boğaziçi Lifesci Pre-Clinic Lab. MR solutions desktop animal CT system.	57
Figure 4.10	Boğaziçi Lifesci Pre-clinic Lab. MR solutions desktop animal CT system workstation.	58

Figure 4.11	Vero Clear - transparent resin and printed spheres.	58
Figure 4.12	Object connect 260 model 3D printer and printed Veroclear-transparent spheres.	59
Figure 4.13	Lifesci Pre-Clinic Laboratory animal CT.	59
Figure 4.14	Caliper device size measurements.	60
Figure 4.15	Istanbul University, Istanbul Faculty of Medicine, NM Department, size measurment of spheres under SPECT-CT.	60
Figure 4.16	Design of outer cylinders.	61
Figure 4.17	Printing of cylinders on Epilog laser printer.	61
Figure 4.18	Preparations of cylinders: (a) cylinders with 2 holes on top; (b) cylinders with 3 holes on top.	62
Figure 4.19	(a)Arpat phantom and cylinders; (b) Spheres in cylinders; (c)Arpat phantom ready to carry on site.	65
Figure 4.20	Preparation of the ARPAT phantom prior to scanning and placement within the scanner.	66
Figure 4.21	Biodex Atomlab 500 dose calibrator and FDG preparation.	67
Figure 4.22	Workstation: GE Advantage Windows processing workstations.	67
Figure 4.23	Arpat in PET-CT.	69
Figure 4.24	Biodex Atomlab dose calibrator.	69
Figure 4.25	Siemens Syngo acqusition workplace processing workstation.	70
Figure 4.26	Arpat is in Philips PET-CT.	70
Figure 4.27	FDG preperation and injection.	71
Figure 4.28	Extended Brilliance Workspace (EBW) processing workstation.	72
Figure 4.29	Arpat in digital PET-CT.	73
Figure 4.30	FDG preperation and injection.	73
Figure 4.31	Advantage Windows processing workstation.	74
Figure 4.32	Cylinders for reference scan.	76
Figure 5.1	Recovery coefficients as a function of the diameter of spheres for all sites.	82
Figure 5.2	Variation of RCs with tumor sizes (spheres) in the thorax region for n values (a) n=4:1 and (b) n=8:1 for all four sites.	84

Figure 5.3 Variation of RCs with tumor sizes (spheres) in the abdomen region for n values (a) n=4:1 and (b) n=8:1 for all four sites. 84

Figure 5.4 Variation of RCs with tumor sizes (spheres) in the pelvis region for n values (a) n=4:1 and (b) n=8:1 for all four sites. 84

LIST OF TABLES

Table 2.1	Positron-emitting radionuclides, physical half-lives, and production methods.	11
Table 2.2	PET imaging agents and applications.	12
Table 3.1	PET scintillator crystals and specifications.	17
Table 4.1	PET-CT scans and their locations.	49
Table 4.2	General Electric-GE Discovery IQ-4 PET-CT specifications	66
Table 4.3	Siemens Biograph mCT 20 PET-CT system specifications.	68
Table 4.4	Philips GEMINI TF 16 PET-CT system specifications.	71
Table 4.5	GE Discovery MI Digital PET-CT system specifications.	74
Table 4.6	Scan parameters.	75
Table 4.7	Dose parameters.	75
Table 5.1	For acquisitions at n=4:1 and n=8:1, RC values for each anatomical region and each sphere for site-1.	80
Table 5.2	For acquisitions at n=4:1 and n=8:1, RC values for each anatomical region and each sphere for site-2.	81
Table 5.3	For acquisitions at n=4:1 and n=8:1, RC values for each anatomical region and each sphere for site-3.	81
Table 5.4	For acquisitions at n=4:1 and n=8:1, RC values for each anatomical region and each sphere for site-4.	82

LIST OF SYMBOLS

c	Speed of light
cc	Cubic centimeters
Ci	Curie
E	Energy
gm	Gram
kg	Kilogram
m	Mass
ns	Nanoseconds
$T_{1/2}$	Half life
β	Positron
ν	Neutrino

LIST OF ABBREVIATIONS

APD	Avalanche Photodiodes
ART	Alderson Radiation Therapy
BGO	Bismuth Germanate
CTAC	CT-based attenuation correction
EIC	International Electrotechnical Commission
FDG	Fluorodeoxyglucose
FOV	Field Of View
FWHM	Full Width at Half Maximum
LOR	Line Of Response
LSO	Lutetium Oxyorthosilicate
LYSO	Lutetium Yttrium Orthosilicate
NEMA	National Electrical Manufacturers Association
PET/CT	Positron Emission Tomography /Computed Tomography
PMT	Photomultiplier Tube
PVE	Partial Volume Effect
PVEC	Partial Volume Effect Correction
RC	Recovery Coefficients
ROI	Region Of Interest
RSD	Radiology Support Devices
RT	Radiation Therapy
SiPMs	Silicon Photomultipliers
SNR	Signal-to-Noise Ratio
SUV	Standardized Uptake Value
TOF	Time Of Flight
VOI	Volume Of Interest

1. INTRODUCTION

This dissertation lies within the domain of Nuclear Medicine, focusing on the integrated use of Positron Emission Tomography and Computed Tomography (PET/CT) systems. These hybrid imaging technologies have become increasingly important in both the diagnosis and treatment of various diseases. With the ongoing progress in medical science, the clinical utility of PET/CT continues to grow, introducing new areas of application. In recent years, special emphasis has been placed on its role in detecting small lesions, staging tumors, planning radiation therapy, and monitoring treatment response. The reliability of these procedures heavily depends on the quality of PET/CT images, where accurate quantification is critical for precise diagnosis and effective follow-up.

In this study, images obtained using a customized anthropomorphic phantom across various PET/CT systems from different manufacturers and institutions were utilized. The focus of this work is on oncological evaluation, with particular emphasis on the assessment of small lesions. In the field of oncology, PET/CT imaging is extensively employed to identify areas of malignant cell presence within the body and to assess disease progression throughout the course of cancer treatment. These scans serve as crucial instruments for evaluating the extent of cancer dissemination and informing treatment strategies [1].

In the first phase of this study the design and production of an original anthropomorphic phantom is completed, and RCs, which are one of the PVE correction methods that arise in PET imaging, are determined. In the second phase, the SUV corrected values are calculated for oncological lesions (tumors) using the RCs [2]. This method is intended to be applicable across different PET/CT systems from various manufacturers with diverse technological specifications. Upon completion of this study, the proposed method is expected to make a significant contribution to clinical PET analysis by enabling more accurate determination of the true dimensions of sub-centimeter

small-volume lesions (0.3 cm, 0.5 cm, and 0.9 cm) through effective PVE correction [3]. Additionally, this methodology is expected to trigger preliminary prospective clinical studies, further advancing the capabilities of PET imaging in oncological assessments.

Correction of PVE in PET Systems is the most crucial component of molecular imaging in oncology [4]. In molecular imaging, particularly in oncological PET scans, the challenge arises from small-volume lesions, which can retain a small amount of radioactive material, making it difficult to distinguish them from the back ground activity [5]. As a result, they appear dispersed across a wider region in the reconstructed image, failing to reflect their true volumetric dimensions. These effects, causing potential inaccuracies in the diagnosis of oncological diseases, are referred to as PVE. PVE can occur depending on the size and the geometry of the lesion, spatial resolution of PET scanner detectors produced by different companies, back ground activity around the tissue, and the chosen image and voxel size [6, 7].

In this study, by minimizing PVE, the aim is to contribute to the early diagnosis, monitoring, and accurate therapy planning for cancer through the precise determination of the real dimensions of small-volume oncological lesions.

2. NUCLEAR PHYSICS

In the course of history, physics has been subdivided into various branches following major breakthroughs. Following the discovery of radioactivity, research led to the consideration of nuclear physics as a new subfield within physics. Unlike atomic and molecular physics, nuclear physics delves into the study of the atomic nucleus, its constituents, and the interactions between them. Investigations revealed that radioactivity is a phenomenon distinct from other chemical events.

Nuclear physics is divided into two main branches: theoretical and experimental. The theoretical branch comprises four distinct subcategories, namely nuclear properties, nuclear models, radioactivity, and nuclear reactions. The other major branch of nuclear physics focuses on experiments. The experimental branch explores diverse nuclear properties and strives to develop improved and more powerful technologies for nuclear experiments. This branch consists of two subcategories: accelerators and detectors.

As a result of nuclear physics research, a new field of study has emerged. While developing powerful accelerators capable of splitting nuclei, it has also become possible to examine particles within the nucleus. This development has opened the door to the establishment of a new branch of physics, specifically the field of high-energy and particle physics [8].

Nuclear physics finds extensive application in nuclear medicine, a specialized discipline dedicated to medical imaging and therapeutic procedures [8].

In the diagnostic part of nuclear medicine, radioactive tracers or radiopharmaceuticals (materials tagged with a small amount of radioactive substance) come into play. These tracers are introduced into the body, and we track their distribution using specialized imaging techniques like Single Photon Emission Computed Tomography

(SPECT) or Positron Emission Tomography (PET). These imaging techniques are used in functional imaging and provide valuable insights into how organs and tissues function at the molecular level, targeting in the identification of abnormalities, tumors, and other medical conditions [8].

Nuclear physics also plays an important role in therapeutic applications within nuclear medicine. For example, radiation therapy, a common method for treating certain cancers, involves using targeted radiation to eliminate or derogate tumors. Radioactive isotopes, generated through nuclear processes, allow us to apply precise radiation levels to targeted regions affected by cancer, minimizing harm to surrounding healthy tissues [8].

The fusion of nuclear physics and medicine not only extend our understanding of the complex workings of the human body but also pushes forward the development of advanced diagnostic and therapeutic techniques. This interdisciplinary approach contributes significantly to improving patient care and outcomes, showcasing the practical implications of insights gained from fundamental research in healthcare.

2.1 Nuclear Medican Physics and Radiation

2.1.1 Definition and Types of Radiation

Radiation is characterized as the absorption and transfer of energy within a substance. It can also be described as the dispersal of energy from a radiation source to another medium. This transmission of energy can take the form of particle emissions or electromagnetic waveforms. The various types of energy emerging from atoms in diverse forms and their methods of dissemination collectively fall under the term electromagnetic radiation. Radiations, which encompass X-rays, gamma rays, and visible light, create an electromagnetic spectrum based on their wavelengths and frequencies [9].

2.1.2 Radiation Sources

Radiation sources are classified into two categories: natural and artificial radiation [10].

Natural Radiation: This type of radiation exists in nature without any human contribution. External sources include cosmic radiation and radiation emitted by the radioactive elements present in the structure of rocks and soil on Earth. This radiation, which affects all living beings, is referred to as back ground radiation.

Artificial Radiation: This type of radiation arises from radioactive materials formed as a result of human activities. While natural back ground radiation affects everyone, artificial radiations impact specific individuals at certain times (due to their professions or for diagnostic and therapeutic purposes, etc.).

2.1.3 Types of Radioactive Decay

Radioactive nuclei undergo spontaneous decay to achieve a stable structure. This decay can occur in three different forms: alpha, beta, and gamma decay [8, 9].

Alpha Decay

The emission of alpha particles cannot be accounted for by classical physics, as alpha particles within heavy nuclei such as radium possess insufficient energy to surpass the substantial potential energy barrier. Although the potential barrier may reach values between 30 and 40 MeV, the energies of the emitted alpha particles are consistently observed to be below 10 MeV. However, considering wave mechanics, the de Broglie wavelength of the alpha particle inside the nucleus allows it a probability to pass through the barrier, and this happens. A trapped alpha particle in the nucleus can be thought of as temporarily coming together to form a particle consisting of two neutrons and two protons.

Beta Decay

Beta decay (β decay) If the instability of a radionuclide arises from an excess of neutrons in the nucleus, it converts one of the neutrons into a proton and an electron to alleviate the excess energy in the nucleus. While the proton remains in the nucleus, the electron is rapidly ejected from the atom. This high speed electron is referred to as a beta particle.

Gamma Decay

After emitting radiation either due to excess energy in its nucleus or as a result of nuclear decay, an atom often cannot immediately transition to a stable (ground energy level) state. The newly formed nuclide in the decay is in a semi-stable state. It releases the excess remaining excitation energy promptly in the form of electromagnetic gamma radiation . This type of decay, where there is no change in the atomic and mass numbers of the semi-stable nuclide, is known as isomeric decay.

Radioactivity and Laws of Radioactive Decay

Radioactivity was discovered in 1896 by Becquerel during experiments examining the fluorescence of certain substances activated by sunlight. The observation of traces on a photographic plate left next to uranium salts in a drawer in a dark room led to the idea that certain rays were emitted. It was later observed that these rays ionized the air. These rays were initially called Becquerel rays, and it was later found that similar rays were emitted by other elements. The atoms emitting such rays were termed radioactive atoms, and the phenomenon was named radioactivity. The emission of rays or particles by radioactive nuclei, releasing their excess energy and transforming into another nucleus, is referred to as radioactive decay, and the emitted rays or particles are generally called nuclear radiation [10, 11].

Radioactivity is studied in four main aspects: physical, biological, effective, and average half-life.

Physical half life

Physical half-life, also known as radioactive half-life, is defined as the time it takes for half of the initial radioactive atoms to decay. The reduction in the number of atoms due to their decay is known as radioactive decay. During radioactive decay, the decay rate of the radioactive substance remains constant. The decay rate is unaffected by changes in temperature, pressure, or chemical conditions. While some atoms remain undecayed during radioactive decay, others undergo decay. The ratio of the number of decaying atoms to the number of undecayed atoms remains constant in equal time intervals, and this value is referred to as the decay constant.

Biological half life

The time it takes for the amount of a radioactive substance initially taken into the body to decrease by half through biological pathways (urine, sweat, saliva, respiration, etc.) is known as the biological half-life. The biological half-life is represented by Tb. Radioactive substances taken into the body undergo metabolic processes similar to non-radioactive isotopes.

Effective half life

Radioactive substances taken into the body decay through both physical and biological pathways. Therefore, a third half-life, combining both terms, is mentioned:

The effective half-life is denoted by Te. The effective half-life is generally determined experimentally.

Average half life

The active lifetime of any radioactive atom can range from zero to infinity. However, the average lifetime of a large number of atoms is a finite value. The average lifetime is the reciprocal of the decay constant and represents the average time it takes

for all atoms of an element to decay and transform into another element. The average half-life is equal to 1.443 times the physical half-life. The unique lifespan of a nuclide is associated with the decay constant, and the lifetime is denoted by T. Average lifetime is an important parameter in radiation dosimetry measurements.

Interaction of Radiation with Matter

Electromagnetic radiation primarily interacts with atomic electrons within matter. The mechanism of interaction, the probability of interaction, and energy loss vary depending on the charge, energy, atomic number of the medium receiving the radiation, and the density of the medium [12].

Interaction of Charged Particles with Matter

Radiation transfers energy to the medium it traverses, causing various interactions. The accumulation of energy in the target is defined as the radiation dose, and if the target is living tissue, the result is often undesirable biological changes. Understanding these interactions naturally precedes the determination of units used in radiation exposure and dose definition. The interaction mechanisms of different types of radiation with the absorbing medium form the basis for processes such as determining the stored energy amount, how the distinguishing characteristics of the medium effect radiation position and dose, and radiation detector design.

Radiation, whether in particle or electromagnetic form, involves contributions from energy, mass, momentum, and charge properties when interacting with matter. Various absorption and scattering interactions lead to the excitation and ionization of the medium.

Interaction of Photons with Matter

Photons, such as X-rays and gamma rays, interact with the electrons and nucleus of the atoms in the medium through various ways. However, since they are electromag-

netic waves, mass and charge are not involved, making their interaction mechanisms with the medium quite different from charged particles.

As photons pass through matter, they scatter and/or are absorbed by the material. X-rays or gamma rays slowdown in the material, exhibiting attenuation by losing energy exponentially. In other words, they show a steady decrease as they progress through the material. This decrease depends on the structure and thickness of the material, as well as the energy of the photons.

The photon intensity decreases exponentially with the thickness of the absorbing material, and the intensity of the outgoing radiation depends on the attenuation coefficient and the thickness of the structure.

Radioisotopes and Radiopharmaceuticals Used in PET Imaging

Positron emitters are short half-life ($T_{1/2}$) radionuclides used in PET imaging, and the physical half-lives of radionuclides used in PET imaging vary between 1.3 to 110 minutes. The physical half-life ($T_{1/2}$) is the time required for a radionuclide's initial activity to halve and is characteristic for each radionuclide. The short half-lives of these radioisotopes produced in cyclotrons bring limitations to their supply and use in PET.

The most important feature of radiopharmaceuticals and radionuclides used in PET imaging is that they contain elements such as Carbon (C), Oxygen (O), Fluorine (F), and Nitrogen (N), which are the basic building blocks of the body, and they behave biologically like these molecules.

In PET studies, compounds labeled with Fluorine-18 (18F) are used to a 90 percent extent. The approximately 2-hour half-life of F-18 allows for the procurement and use of imaging agents produced by imaging centers [13].

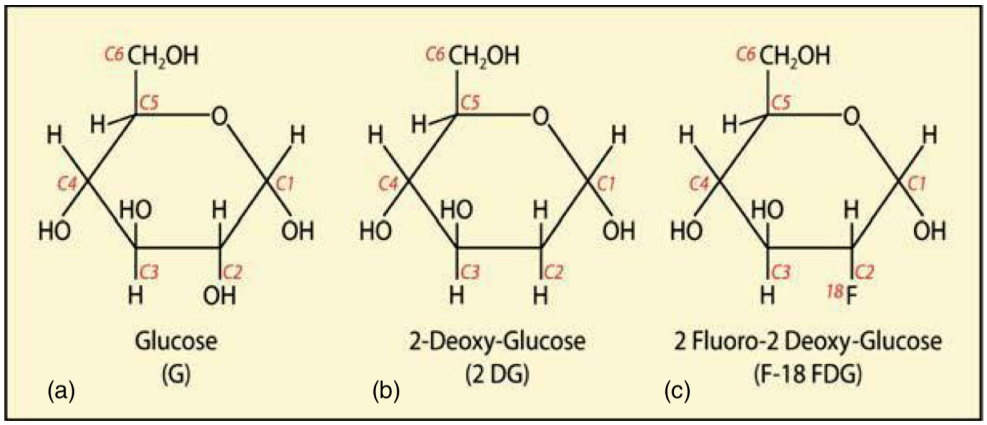


Figure 2.1 Structure of (a) glucose; (b) 2 DG and (c) F-18 FDG [14].

Fluorine-18 Fluorodeoxyglucose (18F-FDG), commonly referred to as FDG, which is a glucose analog labeled with 18F produced in a cyclotron (Figure 2.1). It enters cells through active transport pathways involving GLUT (Glucose Transporter) receptors, similar to endogenous glucose. The GLUT-1 receptor primarily plays a role in the cellular uptake, where FDG enters the cytoplasm. Once inside, FDG-6-phosphate is formed through phosphorylation by the hexokinase enzyme. However, unlike glucose, FDG-6-phosphate cannot progress through the glycolytic pathway because it is not a substrate for the phospho-glucose isomerase enzyme. As a result, FDG-phosphate accumulates within the cell. It is then converted back to FDG by glucose-6-phosphatase and excreted through glomerular filtration in the kidneys without tubular reabsorption, unlike endogenous glucose.

In normal tissues, glucose consumption is regulated by hormonal and intracellular control mechanisms. In fasting conditions, tissues with insulin-dependent glucose transport mechanisms utilize alternative energy substrates like fatty acids or ketone bodies. Hypoxic tissues primarily rely on anaerobic glycolysis as the main energy source, leading to increased glucose consumption [15].

Rapidly replicating cancer cells also heavily depend on glycolysis, a metabolic pathway first demonstrated by Warburg in 1930 [16]. Cancer cells exhibit abnormal glucose consumption even in the presence of sufficient oxygen, attributed to increased

expression of membrane glucose transport receptors and glycolytic enzymes due to genetic mutations [17]. The degree of increase in glycolysis and glucose transport into cancer cells is correlated with tumor aggressiveness and metastatic potential. FDG, exploiting this principle, serves as a unique metabolic agent in tumor imaging.

The physical half-lives and production methods of the most commonly used positron-emitting radionuclides in PET imaging are summarized in Table 2.1.

Table 2.1
Positron-emitting radionuclides, physical half-lives, and production methods.

Radionuclide	Physical Half-life (minutes)	Production Method
Rubidium-82	1.25	Generator
Oxygen-15	2.03	Cyclotron
Nitrogen-13	9.98	Cyclotron
Carbon-11	20.04	Cyclotron
Gallium-68	68.3	Generator
Copper-62	9.74	Generator
Fluorine-18	109.8	Cyclotron

Radionuclides such as ^{11}C, ^{13}N, ^{15}O, and ^{18}F, which have low molecular weights, are cyclotron products, whereas isotopes like ^{62}Cu, ^{68}Ga, and ^{82}Rb are generator products [18]. ^{18}F is preferred for FDG production due to its suitable physical half-life, its ability to be produced in a cyclotron, its energy levels being appropriate for transport and patient dose considerations, and the fact that it does not emit additional radiation [19]. The most widely used PET imaging agents and their applications are listed in Table 2.2. These tables provide an overview of the commonly used radionuclides in PET imaging, their physical characteristics, production methods, and the corresponding imaging agents along with their applications.

Table 2.2
PET imaging agents and applications [18, 19].

Imaging Agent	Application
F-18 Fluorodeoxyglucose	Regional glucose metabolism
F-18 Sodium Fluoride	Bone tumors
C-11 Methionine	Amino acid uptake/Protein synthesis
C-11 Deoxyglucose	Regional brain metabolism
O-15 Oxygen	Oxygen extraction fraction
C-11 Carbon Monoxide	Brain blood volume
O-15 Carbon Monoxide	Brain blood volume
O-15 Water	Brain blood flow
O-15 Carbon Dioxide	Brain blood flow
C-11 Butanol	Brain blood flow
C-11 N-methylspiperone	Dopamine D2, Serotonin S2 receptors
F-18 N-methylspiperone	Dopamine D2, Serotonin S2 receptors
C-11 Raclopride	Dopamine D2 receptors
F-18 Spiperone	Dopamine D2 receptors
Br-76 Bromospiperone	Dopamine D2 receptors
C-11 Carfentanil	Opiate mu receptors
C-11 Flumazenil	Benzodiazepine (GABA) receptors

2.2 Radiation Does Units

Units related to radioactivity have been defined by the International Commission on Radiological Protection. To measure the amount of ionizing radiation, units capable of measuring radiation absorption are needed. Radioactivity units are used for the purpose of measuring radiation and radiation protection. Both old and new units used for this purpose are explained together [20].

2.2.1 Activity Unit (Curie and Becquerel)

Activity expresses the number of transformations of radioactive nuclei per unit time, also defined as the intensity of radioactive emission. For many years, the standard

unit of activity was the Curie (Ci), defined as the emission rate of 1 gram of Radium. 1 Curie is determined as $3.7 * 10^{10}$ disintegrations per second or $2.22 * 10^{12}$ disintegrations per minute. Especially in Nuclear Medicine applications, the Curie unit, representing a large amount of radioactive activity, is used in routine applications, and its submultiples, millicurie and microcurie, are used. Under normal conditions, 1 Ci of 99mTc activity can meet the daily needs of a large-capacity nuclear medicine laboratory.

Activity is defined in the SI unit as the Becquerel (Bq). 1 Becquerel represents the activity of radioactive material that produces 1 disintegration in 1 second. In Nuclear Medicine practice, the Becquerel unit is used in publications. Since the Becquerel defines much smaller amounts of radioactivity compared to the Curie, its submultiples are not used, and the multiples are used.

Between Curie and Becquerel, the following relationships exist:

$$1\ microcurie = 37\ kilobecquerel$$

$$1\ millicurie = 37\ megabecquerel$$

$$1\ Curie = 37\ gigabecquerel$$

2.2.2 Irradiation Unit

Under normal conditions, the amount of radiation that creates (+) and (−) ions in 1 kg of air, producing an electric charge of $2.58 * 10^{-4}$ coulombs, is the irradiation unit. The unit of irradiation is the Röntgen. It is a measure of the ionization of air by radiation. In SI units, the irradiation unit is expressed as Coulomb/kg, equivalent to the Röntgen equivalent.

2.2.3 Absorbed Dose Unit

When radiation is emitted, numerous interactions occur, and energy is deposited in the medium it passes through. The energy absorbed per unit mass is defined as the radiation dose, and if these interactions occur within living tissue, they result in biological changes. Determining exposure to radiation helps understand these interactions, and units guide in defining these interactions.

The absorbed dose represents the energy deposited per unit mass of substance. Traditionally, the rad unit is defined as the storage of 100 ergs of energy in 1 gram of irradiated material. In the SI unit, the absorbed dose is the Gray (Gy), defined as 1 joule of energy deposited per kilogram of the medium. This dose unit shows only the amount of absorbed energy and is applicable to both particle and electromagnetic radiation, encompassing the properties of the absorber material along with the radiation beam.

$$1\ Gray(Gy) = 100\ rad$$

The absorbed dose from 1 Roentgen of radiation in 1 gram of air is 87.6 erg/g, and the air dose is calculated as 0.876 rad (cGy).

2.2.4 Equivalent Does Unit

Biological effects created by different types of ionizing radiation can vary. The degree of biological effects generally depends on the energy loss along the path of radiation per unit distance. The Relative Biological Effectiveness (RBE) is the amount of any radiation that produces the same biological effect as 1 Röntgen of X rays or gamma rays. The traditional equivalent dose unit denoted by H is the Rem, defined as the product of the absorbed dose and the quality factor (Q). In SI units, it is the Sievert (Sv). The types of radiation used in nuclear medicine generally emit gamma and beta rays and are relatively low-energy. As the quality factor for these rays is 1,

dose quantities calculated in rad and rem can be considered equal.

2.3 Fundamental Rules of Radiation Protection

The use of radiation in basic science, agriculture, industry, and medicine has necessitated the development of rules for radiation protection.

Today, the International Commission on Radiological Protection (ICRP) continues its activities since its establishment. ICRP is an independent expert organization, not a government body, and has been recommending "maximum permissible" radiation doses since its founding in 1928. In 1977, in its publication No. 26, ICRP developed new concepts. The concept, named ALARA, is formed from the initials of the words "As Low As Reasonably Achievable". It limited the maximum dose that radiation workers could receive in one year to 50 mSv and imposed a rule that the total dose received within a five-year period should not exceed 100 mSv. Additionally, ICRP set the limit for the dose that the general public could receive to 1 mSv/year in 1990. According to the ICRP recommendations published in 2007, the 1990 recommendations are still valid. However, in Europe (EUROATOM), the annual dose limit is accepted to be a maximum of 20 mSv [12, 21].

2.3.1 Protection Methods Against Radiation

International organizations have established certain rules for external radiation protection. These rules mainly involve factors such as time, distance and shielding (protective barrier) [12, 21].

Time

Since the amount of radiation dose is directly proportional to time, the less time one is exposed to radiation, the lower the dose received. Minimizing the duration

of exposure to radiation is crucial. Radiation workers need to plan their exposure times in advance. Trial-and-error methods can lead to unnecessary exposure to more radiation. Therefore, minimizing the exposure time is a critical strategy to reduce radiation exposure.

Distance

As one moves away from the radiation source, the intensity of radiation decreases inversely with the square of the distance. Therefore, especially for radiation workers, it is essential to adopt the principle of working at a distance as far as possible from the radiation source.

Maintaining a safe distance from the radiation source is a fundamental principle in reducing radiation exposure.

Shielding

The obstacle placed in front of the radiation source to reduce its intensity is called shielding. Different protective barriers are used depending on the type of radiation exposure. Therefore, during exposure, protective equipment such as lead aprons, lead gloves, lead glasses, lead screens, leaded glass, and gonadal shields should be used. Utilizing shielding is crucial in minimizing the impact of radiation exposure and protecting individuals from its harmful effects.

3. BASICS OF PET AND PET-CT IMAGING

3.1 History of Positron Emission Tomography (PET)

In the history of PET, critical factors such as material sensitivity, image resolution, and counting rate in PET detectors were primarily influenced by the choice of detector material. In the mid-1970s, NaI(Tl) stood as the sole option, but its production posed challenges due to its hygroscopic nature. Furthermore, NaI(Tl) exhibited low density and an atomic number constraining the detection of high-energy 511 keV gamma radiation. Despite these limitations, NaI(Tl) proved effective with high light yield and rapid decay time, ensuring satisfactory accidental coincidence timing resolution. Meanwhile, Bismuth Germanate (BGO), though dense with a high atomic number, was not initially considered as a scintillation material for PET [22], as shown in Table 3.1.

Table 3.1
PET scintillator crystals and specifications [22].

Parameter	NaI(Tl)	BGO	LSO
Effective Atomic No	51	78	66
Density (gm/cc)	3.67	7.13	7.4
Decay Time (ns)	230	300	48
Light Output (Na(Tl)=100)	100	15	75

Although Bismuth Germanate (BGO) had served the PET world since its discovery and was used in the production of most PET tomographs for two decades, the advent of Lutetium Oxyorthosilicate (LSO) marked a revolution in PET imaging. While BGO is highly dense, it produces only 15% of the light output of NaI(Tl) and has a relatively slow light decay time of 300 nanoseconds. LSO, on the other hand, has slightly higher density, a lower atomic number, and five times more efficient light output than BGO. The light decay time of LSO is also 7.5 times faster than that of BGO. When combined, these performance characteristics result in a 37.5-fold improvement

in light output and speed compared to BGO.

The discovery and initial crystal growth process of LSO occurred between 1989 and 1992 and was patented on behalf of Melcher by Schlumberger Technology Corporation. CTI obtained the usage rights for these patents in 1995, initiating a challenging development process. In the same year, Melcher joined CTI to lead the development of LSO. The first LSO tomograph for humans was installed in February 1999 at the Max Planck Institute in Cologne, Germany. The HRRT brain tomograph, containing around 120,000 LSO crystals, achieved an approximate 2.5 mm Full Width at Half Maximum (FWHM) cubic resolution.

Since the 2000s, LSO-based tomographs have significantly increased the number of scanned patients without causing a cost increase compared to BGO tomographs. LSO exhibits performance characteristics close to ideal for PET and practically allows whole-body scans. The discovery of LSO is crucial for the development of modern PET devices [22].

3.2 Basic of PET Physics

The particle known as the positron ($\beta+$), also referred to as the antielectron ($\beta-$), is similar in mass to the electron but differs in that it carries a positive charge. Positron-emitting radioactive materials are obtained through bombardment of stable isotopes with charged particles (such as protons, deuterons, or helium nuclei). For this purpose, particle accelerators called cyclotrons are used. In a cyclotron, charged particles are accelerated along a circular path with the help of variable electromagnetic fields and directed towards stable isotopes placed as targets. As a result of this process, stable isotopes in the target become unstable due to an increased number of protons in their nuclei and begin to emit positrons in order to return to stability (Eq. 3.1).

$$proton- > neutron + positron(\beta+) + neutrino(\nu) \tag{3.1}$$

The positron emitted during the reduction process of the atomic nucleus travels approximately 1-3 mm within its surrounding environment until it combines with a free electron present in the environment. After this combination, both particles convert into energy ($E = mc^2$), resulting in two gamma photons with an energy of 511 keV (kilo-electron volts) emitted at a 180^o angle to each other. This phenomenon is termed "Annihilation" [12, 23] and shown in Figure 3.1.

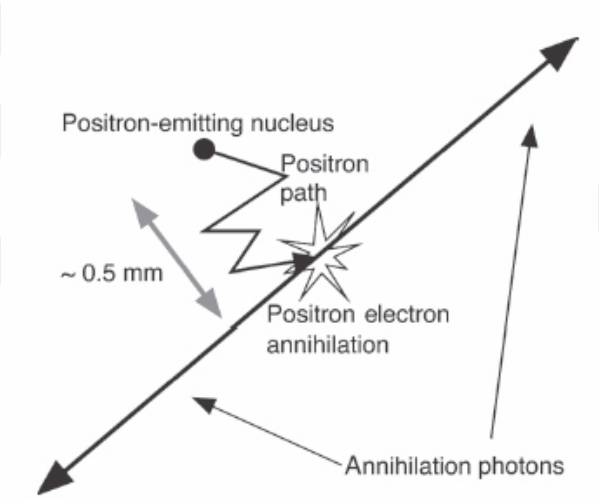


Figure 3.1 Formation of annihilation photons [12].

The distance traveled by the positron until annihilation occurs is an important factor determining the resolution of a PET scanner. An increase in this distance adversely affects the resolution and can lead to quantification errors.

3.2.1 Specifications of PET and PET-CT Scanner

The basic specifications of PET (Positron Emission Tomography) and PET-CT (Positron Emission Tomography-Computed Tomography) scanners can vary depending

on the manufacturer and model. However, here are some common specifications [12, 24]:

1. PET Scanner

    - Detector Type: PET scanners typically use scintillation detectors, such as lutetium oxyorthosilicate (LSO) or gadolinium oxyorthosilicate (GSO) crystals, coupled to photomultiplier tubes (PMTs) or silicon photomultipliers (SiPMs).
    - Spatial Resolution: Spatial resolution refers to the ability of the PET scanner to distinguish between two closely spaced objects. It is typically in the range of 4-6 mm.
    - Axial Field of View (AFOV): AFOV determines the length of the patient's body that can be imaged in a single scan. It typically ranges from 15 cm to 25 cm.
    - Slice Thickness: This parameter refers to the thickness of the image slices reconstructed from the acquired data. Typical slice thickness ranges from 2 mm to 5 mm.
    - Count Rate: The count rate represents the number of detected events per unit time. Higher count rates allow for faster scans and improved image quality.
    - Energy Resolution: Energy resolution measures the ability of the PET scanner to distinguish between different photon energies. It is typically around 10-15% full width at half maximum (FWHM).

2. PET-CT Scanner

    - Combination: PET-CT scanners combine a PET scanner with a CT scanner in a single device, allowing for both anatomical and functional imaging.
    - CT Detector Type: The CT component of a PET-CT scanner uses X-ray detectors to acquire anatomical images.
    - CT Image Resolution: CT image resolution is typically higher than PET image resolution, with voxel sizes ranging from 0.5 mm to 1.0 mm.

- Registration Accuracy: PET and CT images need to be accurately registered to superimpose functional and anatomical information. Modern PET-CT scanners achieve submillimeter registration accuracy.
- Patient Table: PET-CT scanners have a movable patient table that can transfer the patient between the PET and CT components without repositioning.
- Scan Time: PET-CT scans typically take longer than standalone PET scans due to the additional CT acquisition. Scan times vary depending on the protocol and the region being imaged.
- Radiation Dose: PET-CT scans expose patients to radiation from both the PET and CT components. Efforts are made to optimize protocols to minimize radiation dose while maintaining image quality.

These specifications may vary between different models and manufacturers, and technological advancements continually improve the performance of PET and PET-CT scanners [12, 24].

3.2.2 Attenuation Correction

The PET imaging process is subject to several imperfections. Emitted photons can be attenuated as they pass through the patient's body, detection efficiencies can differ among detector elements, and both random and scattered coincidences are registered along with true events. Therefore, various correction techniques are required to produce clinically meaningful images and to ensure the accuracy of quantitative data obtained from PET examinations.

The most important of the corrections is attenuation correction (AC): photons are more likely to be absorbed or scattered (attenuated) when they encounter more or denser materials on their way to the detectors by annihilation than when they pass through more superficial regions of the body (Figure 3.2). If the images are recon-

structed from the sinograms without AC, the less dense regions such as the lungs appear darker (emitting more photons) than the denser tissues such as the mediastinum. This is a clear artifact resulting from the fact that the lung tissue shows less attenuation, not high uptake. It not only distorts the image, but also causes incorrect quantitation of the radiopharmaceutical uptake. To apply attenuation correction, attenuation must be determined over the patient for all LORs. In PET-only devices, this is done by rotating a positron source around the patient and determining the attenuation of the photons by transmission imaging. In PET/CT scanners, CT images are used for PET attenuation correction [24].

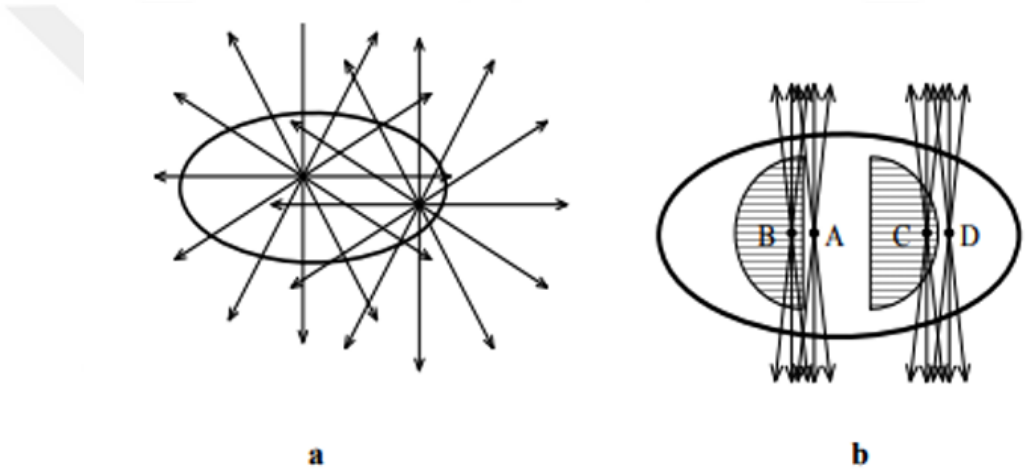


Figure 3.2 Attenuation effect: (a) deeper-more attenuation; (b) brighter-less attenuation [24].

Transmission imaging is done with sources that emit $\beta+$ Ge68/Ga68, single-photon Cs137. When CT is used, Hounsfield values are converted from 140-kVp/ 80 keV to 511 keV.

Computed Tomography based Attenuation Correction

An important adaptation of PET/CT scanners is the use of CT images for attenuation correction of PET emission data. All PET/CT manufacturers use X-ray CT-based attenuation correction (CTAC) algorithms in their systems and it is the only desired option for new PET/CT scanners. CTAC Applied CT data has less statistical noise and is obtained in a shorter time than standard PET transmission imaging,

offering a significant advantage.

CT transmission images can also be acquired after the administration of PET radiopharmaceuticals, allowing for post-injection transmission scans. This approach shortens the patient's time on the scanner bed and improves scanner utilization. For attenuation correction purposes, CT images must be converted into approximate attenuation coefficients at 511 keV. The bilinear scaling method achieves this by applying different scaling factors to bone and soft tissue regions based on the CT data.

Nevertheless, a direct conversion from CT energy levels (around 30 to 140 keV) to 511 keV is not straightforward, primarily because density and atomic number (Z) act as independent variables. As a result, two materials with different atomic numbers may exhibit comparable CT numbers but have distinct attenuation coefficients at 511 keV.

On the other hand, two distinct materials that share the same attenuation coefficient at 511 keV may display different CT numbers, leading to inaccuracies in PET images at the corresponding locations due to CT attenuation correction (CTAC) errors. Such discrepancies often arise when contrast agents or metallic, high-density implants are present in CT scans. Furthermore, misalignments between PET and CT images — for example, those caused by respiratory motion — can also introduce errors into PET data. Therefore, although CTAC significantly enhances PET image quality, artifacts related to contrast agents, metal implants, high-density materials, and motion artifacts may still occur [24].

3.2.3 PET-CT Technology

Positron emission tomography (PET) involves capturing images of radiopharmaceuticals that are labeled with radionuclides emitting positrons. Positrons, which are the positively charged counterparts of electrons, are emitted when a proton-rich nucleus undergoes radioactive decay. In this decay process, a proton transforms into a

neutron, and a positron is ejected with significant kinetic energy. The positron travels a short distance, interacting with surrounding atoms, losing energy, and changing direction. When the positron comes to rest, it annihilates with a nearby electron. Through the conservation of energy, their combined mass energy (rest mass energy; $E = mc^2$) is converted into two annihilation photons, each having an energy of 511 keV (Figure 3.3). According to the conservation of momentum, these two photons are emitted in opposite directions from the point of annihilation. This property forms the foundation of PET imaging, allowing the localization of the original annihilation event within the patient [24].

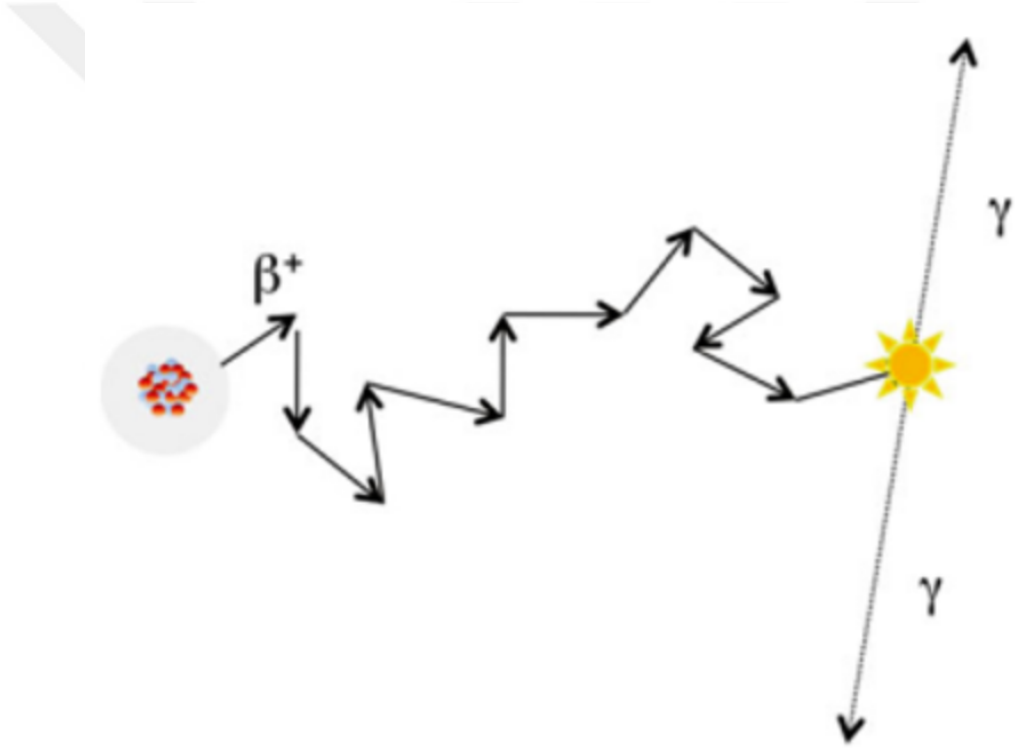


Figure 3.3 Illustration of positron annihilation [12].

A PET scanner consists of multiple concentric rings made up of small scintillation crystals, each only a few millimeters across. These crystals are grouped into blocks, with each block typically connected to four photomultiplier tubes (PMTs). When incoming photons interact with the scintillation crystals, they are converted into light signals, which are subsequently amplified by the PMTs. Following a positron emission within the scanner, two 511 keV photons are produced and detected almost simulta-

neously (within roughly 10 nanoseconds) by different detectors. When two photons are registered within this brief time frame, the event is considered a coincidence. The straight line linking the two detectors that recorded the event is known as the "line of response" (LOR). Over several minutes of scanning, numerous coincidence events are collected and assigned to parallel LORs, which are then used for image reconstruction—commonly through iterative algorithms. A major advantage of PET over gamma camera-based systems is that it does not require mechanical collimators for spatial localization, resulting in significantly greater sensitivity compared to single-photon emission computed tomography (SPECT) [12].

The coincidence event described above, known as a "true" coincidence, is responsible for producing the accurate imaging data. However, other types of undesired coincidence events can also occur (see Figure 3.4). A "random" coincidence arises when multiple positron emissions and subsequent annihilations happen closely in time, leading to photons from different annihilation events being detected within the coincidence time window. If an incorrect pairing of photons is mistakenly identified as originating from a single event, it produces a false line of response. Such an event is classified as a random coincidence because it does not correspond to an actual positron-electron annihilation. The proportion of random coincidences compared to total detected events increases significantly with higher radiotracer activity levels and with the extension of the coincidence timing window, for example, expanding from 10 to 15 nanoseconds [12].

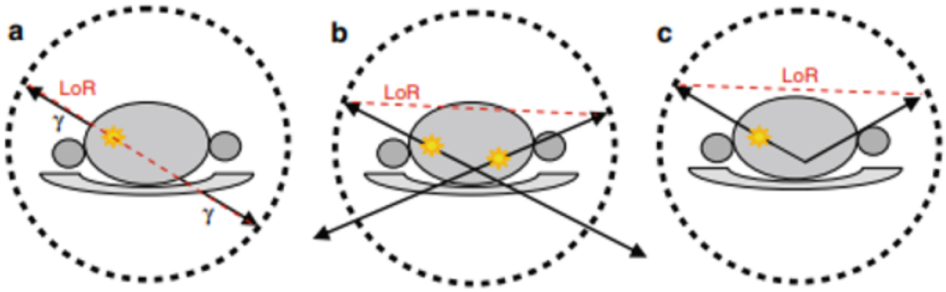


Figure 3.4 Types of coincidence events detected in PET imaging [12]. (a) True coincidence event showing a correct line of response (LoR), (b) Random coincidence event caused by photons from two separate annihilations being incorrectly paired, resulting in a false LoR. (c) Scatter coincidence event where one photon is deflected before detection, leading to a mislocalized LoR.

Scattered events represent another form of error in PET imaging, occurring

when one or both annihilation photons are deflected en route to the detectors, thereby generating an inaccurate line of response. The frequency of these events increases with the presence of more extensive or denser tissues that promote scattering. Although such events can compromise image accuracy, contemporary reconstruction algorithms are designed to compensate for their effects and help preserve image integrity.

In addition to addressing scattered and random events, various other correction steps are implemented during PET image reconstruction to improve overall image accuracy. These include dead time correction to compensate for the loss of data at high count rates, as well as normalization procedures that correct for inconsistencies in detector response along the lines of response.

The most critical correction step in PET imaging is addressing photon attenuation within the patient's body. Although PET photons possess higher energy compared to those used in single-photon imaging, detecting both annihilation photons is necessary to register an event. Consequently, the amount of tissue each photon traverses affects the likelihood of detection, making photon attenuation a significant factor influencing signal strength across different regions. Compared to SPECT, attenuation effects in PET are more substantial, often resulting in uncorrected images that display artificially intense regions, such as the skin and lungs (Figure 3.5) [12].

Generating an accurate attenuation correction (AC) map is key to minimizing the effects of photon loss in PET imaging. The integration of PET and CT technology has greatly facilitated this process, as CT scans—providing detailed attenuation information at X-ray energies—can be rapidly converted into maps suitable for 511 keV photon correction. In PET/CT systems, the patient is imaged sequentially in the same gantry, ensuring alignment between functional and anatomical data. However, several challenges accompany CT-based AC, including the difficulty of accurately scaling attenuation values from X-ray energies to 511 keV, potential image misalignment due to patient movement or respiration, distortions caused by contrast agents or metallic implants, and additional radiation dose from CT. Despite these limitations, CT-derived attenuation correction is widely adopted due to its low noise levels and the

added benefit of anatomical detail, significantly improving the interpretation of PET images [12, 24].

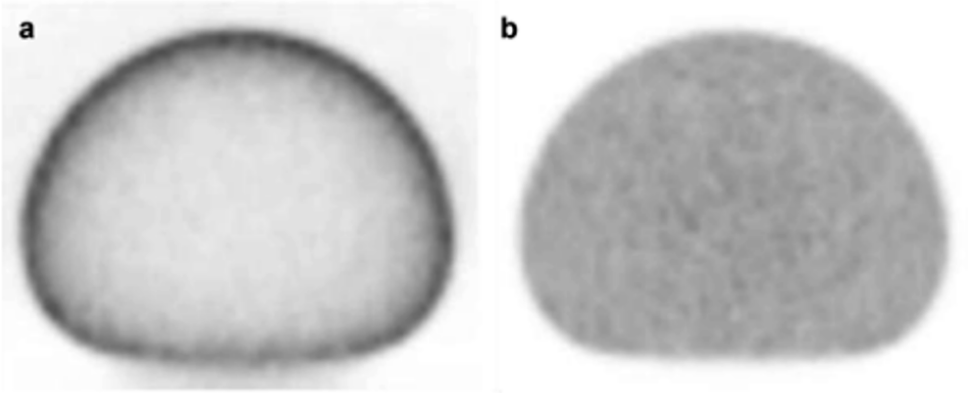


Figure 3.5 Transaxial PET images of a phantom uniformly filled with Fluorine-18 solution: (a) without photon attenuation correction, and (b) after applying attenuation correction [12].

Recent innovations in PET imaging include the integration of point-spread-function modeling during image reconstruction, which significantly enhances spatial resolution and image contrast. Moreover, advancements in fast scintillation detectors have enabled more accurate measurement of the timing of coincident photon arrivals, a method known as Time-of-Flight (TOF) imaging. By narrowing down the possible location of the annihilation event along the line of response, TOF contributes to noise reduction—effectively boosting image sensitivity.

Comprehensive correction procedures in PET-CT facilitate sensitivity calibration, allowing voxel values to be expressed as activity concentration per unit volume (kBq/ml). Since the measured activity concentration can vary depending on patient size and the administered dose, it becomes more meaningful when normalized to the available activity within in the body. Normalizing for the injected activity and patient size (such as body weight or lean body mass) leads to the derivation of the semi-quantitative metric known as the Standardized Uptake Values (SUV). In case of a uniform radiotracer distribution, the SUV of each voxel would be equal to 1.

Initially introduced for whole-body oncological PET imaging, typically utilizing fluorine-18-fluorodeoxyglucose (18F FDG or FDG), PET display workstations typically present images using SUV. Despite its widespread adoption, SUV's accuracy can be

influenced by various factors, necessitating precise measurements of administered activity, injection time, scan time, and patient weight. Additionally, it is impacted by the technical specifications of the PET system and the methods used in image reconstruction. SUV tends to increase proportionally with body weight, particularly affecting larger patients with increased adipose tissue percentages, resulting in increased SUVs in non-fatty tissues [23, 25].

Although normalizing SUV to lean body mass or body surface area reduces dependency on overall body weight, SUV adjusted for body weight remains the most commonly used clinical parameter. Several physiological variables — including the time elapsed between injection and scan, patient resting conditions, body temperature, blood glucose and insulin levels, as well as renal function — can significantly impact SUV measurements. Additionally, since FDG is not a tumor-specific tracer, elevated uptake may occur in regions with infection or inflammation, particularly evident shortly after chemotherapy.

In PET imaging, several SUV metrics can be reported, with SUVmax being the most widely used. While SUVmax is relatively robust and less affected by differences between observers, it is quite sensitive to factors like image noise, the number of detected counts, and the details of image reconstruction. It also may not fully capture the overall uptake in tumors that are heterogeneous. On the other hand, SUVmean offers a better reflection of average tumor activity and is less impacted by noise, but it can vary depending on how the region of interest is drawn, especially when done manually. Even though the SUV formula has its limitations, its simplicity and practicality have made it a mainstay in everyday clinical practice.

PET Detector Technologies

PET detector technologies play a pivotal role in the overall performance of PET systems, impacting sensitivity, spatial resolution, and image quality.

Historically, PET detectors utilized scintillation crystals, such as LSO (Lutetium

Oxyorthosilicate) and LYSO (Lutetium Yttrium Orthosilicate), known for their excellent light output and timing characteristics. Bismuth Germanate (BGO), although offering good stopping power for gamma rays due to its relatively high atomic number, has lower light output and slower decay times compared to LSO or LYSO.

Recent developments involve the optimization of crystal dimensions, improvements in crystal growth techniques, and the exploration of new scintillator materials to enhance energy resolution and timing performance.

Analog PET Technology

Analog PET-CT technology is based on traditional Photomultiplier Tube (PMT) detectors for capturing scintillation events. These detectors convert scintillation light produced by the interaction of positrons and electrons into electrical signals. The analog signals are then processed for image reconstruction. Analog systems may have limitations in timing (PMTs have a finite decay time) and energy resolution compared to digital systems.

Analog PET-CT technology has been widely used in clinical settings and research for molecular imaging, particularly in oncology. It has provided valuable diagnostic information for various medical conditions [26, 27].

Digital PET Technology

Digital PET-CT technology replaces traditional PMTs with solidstate digital detectors, such as silicon photomultipliers (SiPMs) or avalanche photodiodes (APDs). These digital detectors directly convert scintillation light into digital signals for processing. SiPMs have gained prominence as an alternative to traditional photomultiplier tubes (PMTs) for detecting scintillation light. SiPMs offer advantages such as compact size, low power consumption, higher sensitivity and high photon detection efficiency. Ongoing research focuses on optimizing SiPM array designs, enhancing their sensitivity to single photons, and mitigating issues related to temperature dependence and dark

count rates.

Digital PET-CT systems employ solidstate detectors with high sensitivity and low noise characteristics. Digital PET technology provides novel opportunities for more accurate quantification and detailed characterization of small lesions, many of which cannot be identified with analog PET systems. This advancement has the potential to influence patient management strategies and enhance outcomes in both oncological and non-oncological conditions.

In digital PET-CT systems, scintillation signals are directly digitized, allowing for more precise and efficient signal processing. Digital detectors often offer improved timing and energy resolution. Digital PET-CT technology is gaining prominence for its potential to enhance imaging performance. It is utilized in various clinical and research settings, providing improved image quality and diagnostic accuracy [25, 26, 27].

Briefly, both analog and digital PET-CT technologies have contributed significantly to the field of molecular imaging. While analog systems have been widely used and proven effective, digital technology brings advancements in sensitivity, timing resolution, and count rate performance, potentially leading to improved diagnostic capabilities and patient outcomes. The choice between analog and digital PET-CT depends on specific clinical needs, budget considerations, and the desire for cutting-edge technology.

3.2.4 SUV - Standard Uptake Volume and Digitization

The term "Standard Uptake Volume (SUV) / Digitization" in the context of Positron Emission Tomography (PET) refers to a quantitative measure used in the analysis and interpretation of PET images. SUV is a semi-quantitative parameter that provides information about the concentration of a radiopharmaceutical within a specific region of interest (ROI) in the body.

SUV is calculated using Eq. 3.2:

$$SUV\left(\frac{g}{ml}\right) = \frac{Activityconcentration\left(\frac{kBq}{ml}\right)}{\frac{Administeredactivity(MBq)}{Weight(kg)}} \tag{3.2}$$

This formula accounts for the decay-corrected activity concentration in the region of interest normalized by the injected dose and patient-specific factors such as body weight or lean body mass. SUV provides a standardized measure, allowing for comparisons of uptake values across different patients and studies.

The concept of "Digitization" in this context refers to the process of converting analog signals, such as the raw PET image data, into digital format for computational analysis. The digitization process involves discretizing the continuous analog signals into discrete digital values. This transformation is essential for the subsequent quantitative analysis and manipulation of the PET data.

Researchers use SUV to characterize the uptake of radiopharmaceuticals within tissues, aiding in the diagnosis and staging of diseases, particularly in oncology imaging. It helps overcome variations in patient factors, such as body weight, ensuring a more standardized evaluation of PET data. The digitization of PET images facilitates computerized analysis, allowing for precise measurement and comparison of SUV values across different regions of the body [23, 25, 28].

It's important to note that SUV may have variations and limitations influenced by factors such as the type of radiopharmaceutical used, scanner characteristics, and patient-specific variables. Researchers continue to refine SUV methodologies and explore novel approaches to improve its accuracy and reliability in PET imaging.

3.2.5 Partial Volume Effect (PVE)

The Partial Volume Effect (PVE) is a complex process influenced by various factors, including tumor size, shape, back ground activity surrounding the tissue, spatial resolution of the scanner, voxel size, and image selection. Simply put, the PVE occurs when counts obtained from a source are dispersed beyond a region in the reconstructed image that is larger volumetrically than its actual physical dimensions [29].

The primary cause of the PVE is the blurring observed in the three-dimensional image due to the finite spatial resolution of the imaging system. This blurring leads to scattering between regions in the three-dimensional image. In practice, the three-dimensional impact is represented in two dimensions. The image of a small source is larger due to finite spatial resolution. Some of the signals emitted from the source scatter, and thus the actual source is observed.

The second event causing the PVE is the image selection. Radioactive distributions are sampled in a voxel box. The boundaries of the voxels do not match the true boundaries of the radioactive distribution. Many voxels contain different types of tissues. The signal density in each voxel is the average signal density underlying the tissues. Even if the spatial resolution of the imaging system is perfect, the PVE may occur due to image selection. A larger voxel size will result in more PVE. Therefore, voxel density is the average of the activity distributions above the voxel size.

The PVE affects the image qualitatively and quantitatively in two ways. For small-sized hot lesions located in a colder back ground, the PVE emits the signal outward. This effect occurs when the reconstructed image resolution is three times smaller than the FWHM (Full Width at Half Maximum) of the actual tumor size. The maximum value in the hot tumor will be lower than the actual maximum value. A small tumor will appear larger but less aggressive than it actually is [6].

The counterpart of the PVE is somewhat complicated because it involves not only the activity spreading out from inside the tumor but also the case where the

activity outside the tumor is scattered into the tumor. Ultimately, the resulting image is the sum of inward (spill-in) and outward (spill-out) scattering [6].

The outward spillage is clearly related to the retention within the tumor. Generally, they cannot be balanced with inward spillage, so predicting the PVE originating from the entirety is difficult. In tumors partially or completely centered on necrosis, inward spillage will lead to the perception that the cancerous tissue concentrated at the tumor's core is more vibrant than it actually is. Similarly, the tumor may seem less aggressive than it truly is in its active areas [6].

The PVE also affects specific tumor dimensions. This response is particularly controversial when used in PET. Due to the limited spatial resolution of PET imaging (approximately 5 mm), the apparent boundary of a lesion may extend beyond the actual metabolically active tumor region. The discrepancy between the outer boundaries of the tumor is clearly visible in PET/CT. The boundary lines seen in CT do not reveal the metabolically viable tumor tissue. The entirety of the tumoral area with increased radiotracer uptake is only visible in high-resolution functional imaging [4, 30].

3.2.6 Partial Volume Effect Correction (PVEC)

PVE Correction Methods can be categorized into two groups: correction methods based on post-reconstruction and correction methods based on reconstruction. Within each category, there are Region of Interest (ROI)-based and voxel-based approaches. Recent studies have predominantly focused on correction methods based on post-reconstruction.

PVE Correction Methods

The PVEC methods based on post-reconstruction include the following [29, 31, 32, 5]:

1. ROI-Based Correction Methods:

    - RC Method: The use of coefficient improvements is the simplest way to correct the PVE. For a global tumor, the value of RC for a given spatial resolution can be found as a function of the size of the area and the contrast of the area/background. This value is then used for calculations. This method can also be applied to non-global tumors. RC depends not only on the tumor volume but also on the image resolution. The RC value is calculated using the simple formula below. The calculated RC value is then used for correction in the PVE-corrected activity formula. It is important to note that the RC method not only corrects for tumor volume but is also dependent on image characteristics and selection. The calculated RC value is utilized in the PVE-corrected activity formula, especially in the correction of SUV values in PET imaging.
    - Geometric Transfer Matrix (GTM) Method: The GTM method is a technique based on considering a large number of Regions of Interest (ROIs) for the analysis. While the RC method calculates the spread only between two structures (tumor and background activity), the GTM method can calculate the spread between several structures [5].

2. Voxel-Based Correction Methods: These methods define permissible partial volume corrections that can be applied to uptake values within tumors or other regions.

    - Partition-Based Methods: This method, recommended for brain imaging, predicts the accurate pattern of metabolic activity in a series of non-overlapping sections, excluding the region of interest, with known uniform uptake. This method proves valuable for assessing variations in tracer uptake across the tumor, offering the benefit of generating corrected images within the regions of interest by compensating for PVE.
    - Iterative Deconvolution Methods: Deconvolution is used in image restoration, improving spatial resolution. It successfully predicts the scattering effect caused by the Point Spread Function (PSF). The iterative deconvo-

lution technique is used for this purpose. In comparison to RC and GTM approaches, a key strength of this method lies in its independence from any presumptions regarding tumor dimensions, delineation, internal uniformity, or surrounding background activity. However, it requires a known local spatial resolution of 1 mm. This approach is not suitable for improving uptake values in tumors with a diameter 1.5 times smaller than the Full Width at Half Maximum (FWHM) in reconstructed images. For tumors with a diameter 1.5 times larger than FWHM, uptake values are fully improved when obtained from uncorrected images with maximum or average values. The primary challenge associated with deconvolution is the significant amplification of noise. Correction allows for larger noise, providing images unsuitable for visual interpretation. Another issue with deconvolution is the appearance of ring artifacts in regions where sharp density changes occur.

- Multi-Resolution Approach: It predicts the high-resolution image that perfectly represents the obtained SPECT or PET image. There should be no truncation in the high-resolution image. This feature is an advantage over the partition correction method [5].

- Fitting Method: With this technique, it is assumed that there is a spherical tumor in an environment with uniform background activity. The acquired image may be represented as the result of convolving a sphere with a point distribution function assumed to have local spatial resolution. To determine the model parameters—namely, the location and size of the sphere, its uptake, and the background activity—optimization techniques are employed to suppress implausible outcomes by utilizing objective functions with suitable characteristics. One of the key benefits of this method is its ability to adapt the local point spread function based on the anatomical or functional characteristics of the target structure.

- Kinetic Modeling: PVEC may include some kinetic techniques. This method finds application in both cardiac and neurological imaging. When partial volume effect is eliminated, this model includes many parameters that need to be predicted. This approach is applied because it uses limitations intro-

duced by the kinetic model to determine the size of the PVE.

3.3 PET Calibration and Phantoms

Calibrating PET imaging involves ensuring accurate and consistent measurement of radioactivity concentrations, which is crucial for quantitative analysis and comparison of PET images across different scanners and imaging sessions. The calibration process aims to relate the measured PET values (in standardized units like SUV) to the actual radioactivity concentrations in the imaged tissues. Accurate calibration is essential to maintain reliability in multi-center studies and to ensure that quantification remains valid across different equipment and protocols.

Accurate PET calibration requires consideration of several key elements. In the following subsections, the concepts of standardization, the use of SUVs, the role of calibration phantoms, and the methodology of phantom studies are outlined.

3.3.1 Standardization and SUV

The most common metric used for quantification in PET imaging is the SUV. It provides a normalized measure of radioactivity concentration within a region of interest and is critical for clinical and research applications where comparative analysis is needed. To convert PET values into SUV, a calibration factor is required, which is typically determined by imaging a phantom containing a known concentration of radioactivity. Proper determination of this calibration factor ensures that SUVs accurately reflect true biological activity.

3.3.2 Calibration Phantoms

Calibration phantoms are specially designed objects used to establish a reliable relationship between PET scanner measurements and true radioactivity concentrations. These phantoms are constructed with compartments filled with predefined and traceable concentrations of radioactive material. The range of concentrations within the phantom should ideally match the expected in vivo radioactivity concentrations encountered during clinical imaging, thus allowing a realistic and clinically relevant calibration process.

3.3.3 Phantom Studies

Phantom studies typically involve a systematic process encompassing acquisition, analysis, and application of correction factors. During the acquisition phase, the calibration phantom is scanned using the PET system under standardized conditions. In the analysis phase, PET signal intensities within the phantom compartments are measured and compared against the known radioactivity concentrations. If discrepancies are identified, correction factors are applied to address sources of error such as attenuation, scatter, and partial volume effects, thereby improving the quantitative accuracy of PET imaging.

To further standardize and validate PET system performance, specific types of phantoms are employed. Among these, PET-NEMA phantoms and anthropomorphic phantoms are widely used for the evaluation, calibration, and quality control of PET imaging systems, as they provide standardized and reproducible conditions that closely mimic clinical and experimental settings.

PET-NEMA Phantoms

In routine nuclear medicine imaging, standardized PET-NEMA body phantoms featuring a uniform structure are utilized for calculating PVE. NEMA (National Elec-

trical Manufacturers Association) is an organization dedicated to developing methods and protocols for standardizing and assessing the performance of medical imaging devices. NEMA has designed standard phantoms for quality control in PET imaging systems, aiming for their applicability across the industry, notwithstanding potential variations between manufacturers [33].

These NEMA body phantoms replicate the physical and radioactive properties of the human body, encompassing areas resembling various organs, radioactive activity distributions, and diverse tissue characteristics. The application of standard test protocols using these phantoms allows for the assessment of PET imaging system performance, facilitating the comparison of acquired data. These phantoms play a pivotal role in activities such as measuring performance parameters like resolution, contrast, exposure time, and dosage accuracy of PET systems, calibrating imaging systems, determining sensitivity, calculating RC values, and comparing imaging performance. This role is crucial for enhancing the performance and standardization of PET imaging devices.

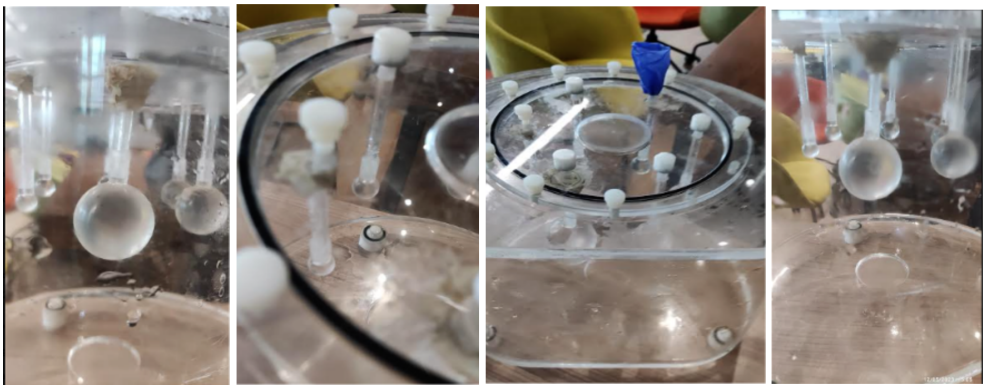


Figure 3.6 PET-NEMA/EIC body phantom spheres in 10, 13, 17, 22, 28, and 37 mm sizes.

Within the NEMA Body Phantom, spherical particles simulating lesions of different sizes (e.g., 1, 1.3, 1.7, 2.2, 2.8, 3.7 mm) are embedded in Figure 3.6. Using radioactive sources, these particles generate target regions with known activity densities. An illustrative example is presented in Figure 3.7 below.

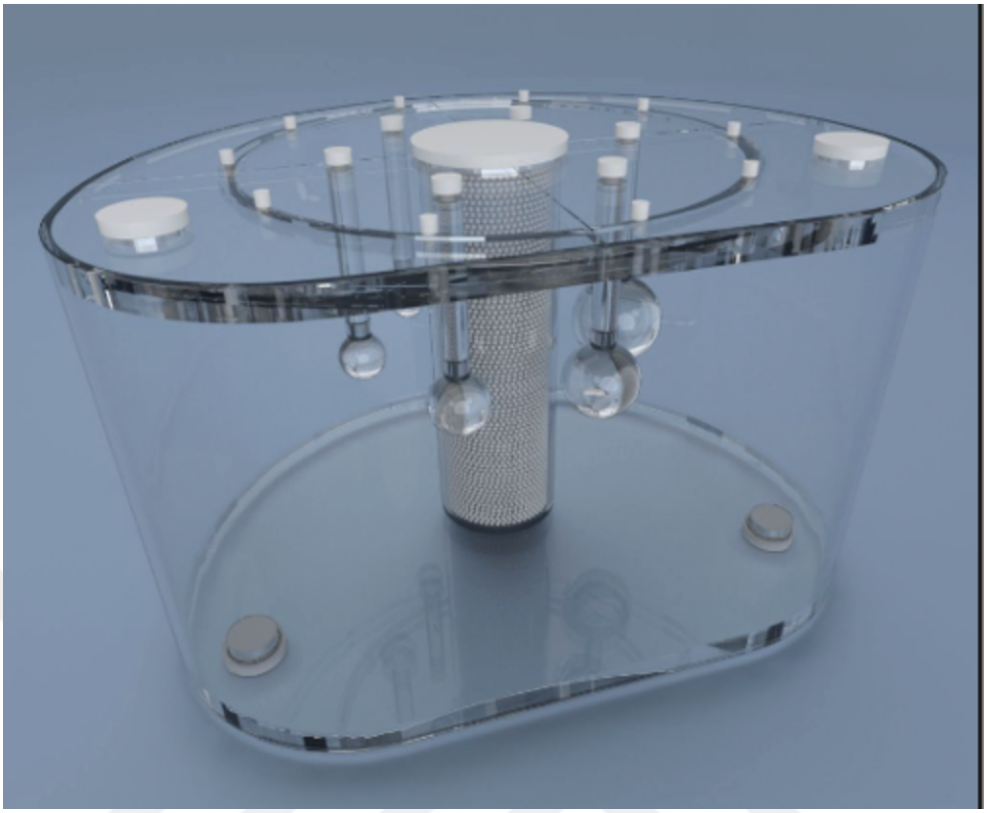


Figure 3.7 PET-NEMA body phantom [33].

The dimensions of the particles used in the PET-NEMA Body Phantom are standardized. According to NEMA specifications, the diameter of particles within the phantom can typically range from 1 to 10 mm. The diameter of these particles may vary in different regions of the phantom.

For instance, particles with smaller diameters may represent high-resolution areas, while those with larger diameters may represent low-resolution areas. However, it's important to note that PET-NEMA specifications can vary from manufacturer to manufacturer and depending on the intended use. In Figure 3.8(a), the PET-NEMA/IEC phantom is illustrated, Figure 3.8(b), depicts a body phantom and its components, and Figure 3.8(c) displays fillable cylinders.

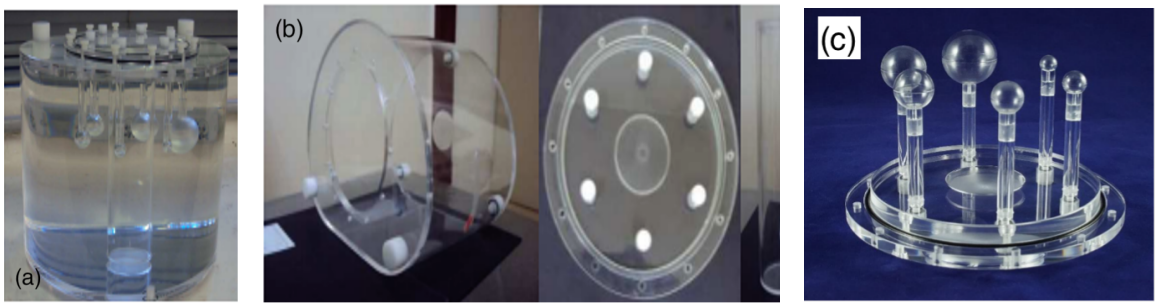


Figure 3.8 Phases of the phantom production (a) PET-NEMA/IEC phantom; (b) PET-NEMA body phantom (torso) - frontal cover and inner cylinder; (c) Fillable cylindrical spheres [33].

As an integral part of scientific investigations in the realm of PET, the utilization of standard PET-NEMA body phantoms filled with water is a common practice. This choice is rooted in the desire to establish a homogeneous structure within the phantom for the purpose of conducting accurate and reproducible studies. The homogeneity of these phantoms is pivotal in conducting PVE measurements, where photons emitted from the radionuclide navigate through a consistent medium before reaching the detector.

In the context of studies conducted with PET-NEMA body phantoms, it is a customary practice to consider tissues within the phantom as having water equivalence. Consequently, all dose calculations pertaining to tumor regions are executed with reference to the properties of water. However, it is crucial to acknowledge that these studies, while valuable in their standardized approach, may not fully encapsulate the inherent complexity of the human body.

Notably, research has illuminated the fact that the human body exhibits an inherent heterogeneity with varying densities compared to a homogeneous water-filled phantom [33]. This inherent diversity in human tissue composition becomes particularly relevant in clinical PET imaging scenarios. In real-world clinical applications, photons emitted from radionuclides within the human body undergo interactions with tissues of differing densities, including adipose tissue, bone tissue, and other anatomical structures, before reaching the detector.

The discrepancy between the standardized measurements obtained using the PET-NEMA body phantom and the real-world complexities of the human body introduces a layer of nuance to the interpretation of PET imaging results. The pursuit of scientific understanding in this field involves navigating these intricacies and recognizing the limitations of standardized phantoms when extrapolating findings to the diverse and dynamic landscape of clinical PET imaging.

Below, in Figure 3.9, the positioning of the PET-NEMA phantom during a PET scan can be observed.



Figure 3.9 Positioning of the PET-NEMA phantom in a PET scan.

The use of materials exhibiting PET and MRI properties similar to human tissues encourages the testing of clinical protocols for application to patients. Consequently, this promotes better compatibility with systems such as radiotherapy treatment planning or dosimetry software [34, 35].

Anthropomorphic Phantoms

Anthropomorphic phantoms are specially designed test mannequins primarily employed to assess the performance of devices used in Radiotherapy, optimize treatment plans, and conduct dosimetry (dose measurement) studies. These phantoms are crafted to mimic the anatomical structure and characteristics of the human body. In Figure 3.10 below, examples of some ATOM Dosimetry phantoms produced by CIRS can be observed [36].

The application of anthropomorphic phantoms in scientific research and medical settings plays a crucial role in evaluating the accuracy and efficacy of radiation therapy devices. By closely emulating human anatomy, these phantoms enable researchers and practitioners to simulate realistic treatment scenarios, ensuring that the performance of radiotherapy equipment is thoroughly assessed under conditions that mirror actual clinical applications.

Moreover, these phantoms serve as invaluable tools for optimizing treatment plans, allowing healthcare professionals to fine-tune radiation doses for maximum therapeutic effect while minimizing potential risks to surrounding healthy tissues. Dosimetry studies conducted with anthropomorphic phantoms contribute to the advancement of radiation therapy techniques and methodologies.

In Figure 3.10, the ATOM Dosimetry phantoms exemplify the design and meticulous construction involved in creating anthropomorphic models for dosimetric purposes. The variety in these phantoms allows for a comprehensive examination of different anatomical regions and treatment scenarios.

The use of anthropomorphic phantoms, such as those produced by CIRS, underscores the commitment to precision and realism in medical research, ultimately contributing to the ongoing enhancement of radiotherapy practices for the benefit of patient care and treatment outcomes [37].

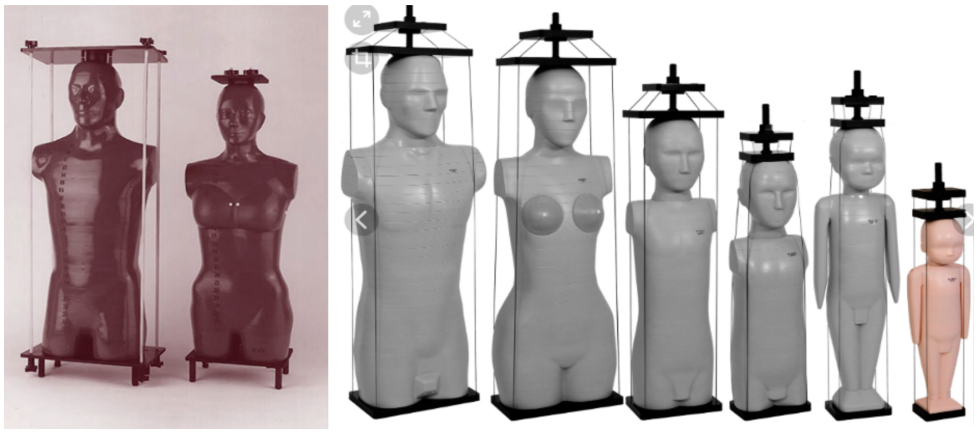


Figure 3.10 CIRS ATOM dosimetry phantoms [36].

Radiotherapy is a method used in cancer treatment, typically employing high-energy radiation to destroy or control cancer cells. In radiotherapy, efforts are made to deliver as high a dose of radiation as possible to cancer cells while minimizing damage to surrounding healthy tissues.

Anthropomorphic phantoms are utilized for various purposes in the field of radiotherapy, including treatment planning, measurement of radiation doses, and testing the calibration of treatment devices. These phantoms provide a realistic model of the human body, incorporating different organs, tissues, and anatomical details. In the planning stage of radiotherapy treatment, simulations can be conducted using these phantoms to optimize factors such as treatment dose, radiation targeting, and the extent of exposure to healthy tissues.

Moreover, phantoms are employed to ensure the accurate and appropriate functioning of treatment devices. Tests can be conducted to ascertain whether the radiation targeting of the radiotherapy device is accurate, if the radiation dose is uniformly distributed, and whether dosimetry measurements yield accurate results. These tests collectively contribute to ensuring the safe and effective application of radiotherapy.

In essence, anthropomorphic phantoms serve as crucial tools to enhance the quality of radiotherapy treatment, minimize side effects, and improve treatment outcomes. These phantoms not only support research in the field of radiotherapy but also contribute to the development of new treatment techniques and methodologies. An example related to anthropomorphic phantoms used for pediatric purposes is illustrated in Figure 3.11 below.



Figure 3.11 Pediatric anthropomorphic training phantoms [36].

When examining the conducted studies, it is concluded that the use of anthropomorphic phantoms, designed to resemble a human-like structure in an inhomogeneous environment [37], in Nuclear Medicine, will reduce the associated error rates, which cannot be achieved by NEMA Body phantoms. However, until now, when scanning the referenced studies related to the use of anthropomorphic phantoms in Nuclear Medicine [37], it has been observed that these phantoms, initially designed for Radiotherapy purposes. They could not be used in the field of Nuclear Medicine for studies detecting small lesions due to their current designs, as they could not accommodate sub-centimeter-sized radioactive substances, such as 3mm, 5 mm, as was desired.

Classical anthropomorphic human body phantoms designed for radiation therapy (RT) are typically produced in sections or modular components (e.g., head-neck, thorax, pelvis) to more accurately replicate the human body and its diverse tissue properties. Among the most recognized phantoms in the market are the Alderson Radiation Therapy (ART) anthropomorphic phantoms, developed by Radiology Support Devices Inc. (RSD) for use in radiotherapy. Initially, the plan was to purchase and modify an ART phantom for this project. However, due to the high costs of these phantoms (ranging from approximately 25,000 to 75,000 USD, depending on the selected modules), it was decided to design and manufacture a custom-built phantom locally, offering a more cost-effective alternative. This locally produced phantom is

also intended to enable its potential use in clinical settings in the future. Figure 3.12 illustrates the ART phantom [36].

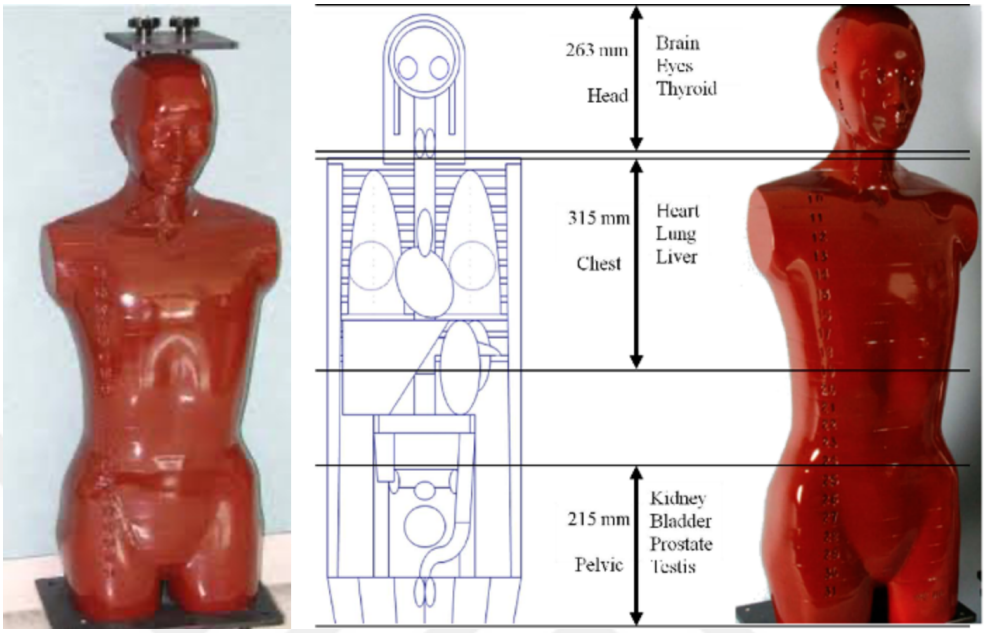


Figure 3.12 Alderson anthropomorphic radiation therapy phantom [36].

In summary, the advantages of using anthropomorphic phantoms in PET imaging include accurate simulation of human anatomy, standardized manufacture and material properties, and reproducibility. However, the disadvantages include limited availability, cost, and complexity in design and development.

3.3.4 Cross Calibration

PET scanners from different manufacturers or even different models from the same manufacturer may produce different PET values for the same radioactivity concentration. Cross-calibration studies aim to harmonize measurements across different scanners, ensuring consistency in SUV measurements.

3.3.5 National Electrical Manufacturers Association (NEMA) Standards

The NEMA standards provide guidelines for PET system performance measurements, including calibration. NU 2-2018 outlines procedures for evaluating PET scanner performance using various phantoms [38].

3.3.6 Quality Control

Regular quality control tests are performed to ensure the ongoing accuracy and reliability of the PET scanner. Normalization procedures may involve daily, weekly, or monthly calibrations to maintain accuracy.

4. MATERIAL AND METHODOLOGY

4.1 Introduction

The aim of this study is to compare tumor and back ground simulations created in 6 different sizes of tumors using an Anthropomorphic phantom on 4 different PET/CT systems, with and without scatter values in 3 different regions (Thorax, Abdomen and Pelvic). Additionally, the goal is to obtain RC values for each device in the 6 different sizes. This way, the standardization of tumor uptake values obtained through PET imaging in patients is intended. The comparison of semiquantitative and quantitative values obtained from PET images of the same phantom (patient) at different time intervals and different centers will assist us in achieving results that are closest to reality.

In this study, a new Anthropomorphic phantom were re-designed to align with the project objectives. The aim is to calculate more accurate RC values, especially for small-volume lesions, by correcting the PVE in Oncologic PET imaging. The ultimate goal is to achieve more precise detection of lesions with dimensions closer to reality. This would contribute to early diagnosis in cancer, facilitating accurate treatment planning and follow-up.

The locally developed Anthropomorphic phantom incorporates cylinders placed within a 5.4 cm diameter hole, designed as spheres positioned on 5 cm diameter, three Plexiglas cylinders positioned at once inside the opened hole to get scan from Thorax, Abdomen and Pelvic regions simultaneously. In order to simulate spill-in and spill-out applications, spheres mimicking lesion sizes were prepared in various volumes (0.3, 0.5, 0.9, 1.3, 1.9, 2.8 cm) and located in these cylinders.

With the developed phantom, the goal was to perform clinical scans on three different PET systems and the latest technology Digital PET System with varying de-

tector structures, launched by different manufacturers and installed in different clinical centers.

For this purpose, necessary permissions/approvals were obtained from relevant authorities. PET scans were performed at Istanbul University Faculty of Medicine Hospital on GE's Discovery IQ-4 Model PET-CT System, at Medipol University Hospital on Philips' GEMINI Model PET-CT System, at Istanbul Training and Research Hospital on Siemens' Biograph mCT Model PET-CT System, and at Prof. Dr. Cemil Taşçıoğlu City Hospital (Ok Meydanı Training and Research Hospital) on GE's Discovery MI Digital PET-CT System which has the latest PET-CT Technology in the industry. The scans were conducted with the original Anthropomorphic phantom developed within the scope of the project, for each spheres (a total of 6), separately, in a clinical setting. Table 4.1 below provides information about the PET-CT scans and their locations.

A total of 72 scans conducted, with three scans for each spheres in the 'Thorax,' 'Abdomen,' and 'Pelvis' regions ($24 * 3 = 72$ scans in total has taken). Since study has performed for both in 4:1 and 8:1 activity ratios; The total number of scans for 4:1 and 8:1 is $72 * 2 = 144$ scans. Furthermore, phantom free (only cylinders with spheres) reference scans has taken for each sites seperately which makes 4 (sites) x2 (4:1 and 8:1 ratios)= 8 additional scans. Totally makes 152 radioactive scans.

After performing phantom imaging studies in different hospitals, the effects of different detectors and technologies developed by various manufacturers, were systematically examined by calculating RCs for PVE correction from each site separately.

In contrast to the PET-NEMA phantom (homogeneous) routinely used in Nuclear Medicine, this study evaluates the effects of a more realistic phantom that takes into account different tissue attenuations from various regions of the body. The calculated RCs are expected to mitigate the PVE observed in millimeter-sized lesions, such as 0.3 and 0.5 cm, by assessing the impacts of realistic human-like phantom (heterogeneous) effects.

Table 4.1
PET-CT scans and their locations.

Sites where PET-CT scans performed	PET-CT System	Model	Sphere diameters for the 1st scan (cm)			|Sphere dimaters for the 2nd scan (cm)			Total
1- Istanbul University- Istanbul Medical Faculty	GE	Discovery IQ-4 Model PET-CT	0.3	0.5	0.9	1.3	1.9	2.8	6
2- Medipol University- MEGA Hospital	Philips	GEMINI Model PET-CT	0.3	0.5	0.9	1.3	1.9	2.8	6
3- Istanbul Training and Research (IEAH) Hospital	Siemens	Biograph mCT Model PET-CT	0.3	0.5	0.9	1.3	1.9	2.8	6
4- Prof.Dr.Cemil Taşçıoğlu City Hospital (Ok Meydanı Training and Research Hospital)	GE	Discovery MI Digital PET-CT	0.3	0.5	0.9	1.3	1.9	2.8	6
Total Scan			4	4	4	4	4	4	24

This study aims to contribute to early cancer diagnosis, monitoring, and accurate therapy planning by determining the true dimensions of oncological lesions.

4.2 Design, modification and production of an anthropomorphic phantom for PVE correction

Due to the unavailability of locally produced Anthropomorphic phantoms for our thesis work and the high cost of procurement from abroad due to limited supplier, a decision was made to custom-manufacture one for our study in house. To achieve this, we started with the production of a alike phantom previously locally produced for dosimetric nuclear studies for a different thesis topic [39]. It is re-designed and modified to suit our study's specific requirements, and the new production Anthropomorphic phantom was carried out accordingly and named as ARPAT (see Figure 4.1). The name was uniquely designated by the project team and does not represent an acronym; rather, it serves as a project-specific identifier for the anthropomorphic phantom. The necessary FDG activity uptake measurements for the thesis were performed on this newly created heterogeneous Anthropomorphic phantom Arpat.



Figure 4.1 Re-designed and modified anthropomorphic body phantom.

During the creation of the phantom, attention was paid to ensuring that the

dimensions and CT numbers of tissues and the skeletal system mimic real human dimensions and CT numbers as it has studied in the reference. Before determining the materials to mimic tissues, the tissue densities of organs such as the liver, lungs, bones, and kidneys were identified based on real human dimensions and CT numbers [39]. In the determination of organ density, in literature studies related to the respective organs indicated that the density of the lungs is approximately 0.3 g/cm^3, organs is approximately 0.90-1.05 g/cm^3, and bones are in the range of 0.96-1.4 g/cm^3.

Additionally, as seen in Figure 4.2 below, the CT numbers of tissues were determined from the CT images of many patients and the human-like vertebra phantom. It was given by the reference study that bone tissues have CT numbers in the range of 200 to 700 Hounsfield Units (HU), soft tissues have CT numbers in the range of -20 to 80 HU, and lung tissue has CT numbers in the range of -700 to -800 HU [39].



Figure 4.2 Human-like vertebra phantom

The body shape and measurements of the phantom, designed in SolidWorks, the initial raw drawings were created by determining the two-dimensional scale (Figure 4.3) by using the SolidWorks program in the cleanroom facility of Boğaziçi University's Life Sciences and Technologies Application and Research Center (Boğaziçi LifeSci).

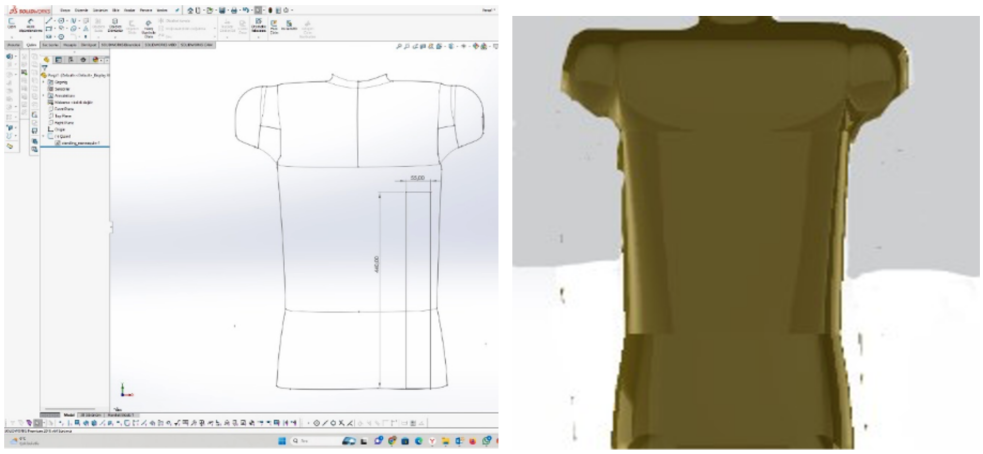


Figure 4.3 Solidworks of 2D raw drawings of anthropomorphic body phantom.

An adult human skeleton model was obtained for the construction of the bone structure (see Figure 4.4(a)). Due to the impossibility of molding the entire skeleton in a single step, all the bones of the skeleton were separated, and the phase of creating molds for the phantom was initiated. Molding was performed using mold silicone (see Figure 4.4(b)).



Figure 4.4 (a) Human skeleton; (b) The adult human model.

The bones of the thoracic, abdominal, and pelvic regions, which will be used in

the measurements, were separated into individual pieces, and each bone was molded separately.

Later, a mixture yielding a value of 550 Hounsfield Units (HU) was prepared. The material, which was measured to be equivalent to bone density, was poured into the molds, creating bones for the entire body as it has done in reference study. To avoid density differences in the obtained bones, the bones were combined using the material produced for bone fabrication, and they were shaped into the skeletal form to be used in the phantom.

The density of lung tissue in the literature was found to be 0.3 g/cm^3 (-700 HU to -800 HU). To simulate the lungs, the lung section of the phantom was left empty, and after the phantom was completed, it was filled from above with styrofoam and water. To achieve a resemblance to human anatomy, the dimensions of a normal-sized patient were utilized from CT cross-sectional images in the literature to simulate the lungs. Three-dimensional lung molds were created from patient image sections, and a three-dimensional lung was formed using styrofoam.

After constructing the internal structure of the phantom, the foam mold created for the lungs was placed within the skeletal framework. The prepared lung skeleton was placed inside the model used for the mold, and to enable the placement of activity within the phantom during measurements, a Plexiglas tube hole with an inner diameter of 5,4 cm was prepared for plexiglas sphere holders. To create soft tissues, a material suitable for 80 Hounsfield Units (HU) was formed using a mixture of epoxy resin, polyester, and various polymers, and it was poured into the mold model. To simulate the tissue density of the lungs, styrofoam was filled into the lung cavities to a volume ratio of 2/3, and the remaining part was filled with water. After this process, the construction of the phantom was completed as in the reference study (see Figure 4.5) [39].



Figure 4.5 Anthropomorphic body phantom Arpat and the hole for the plexiglass spheres placement.

Subsequently, with the aim of completely differentiating our project from the reference work, the design and production of cylinders and spheres (simulated lesions) were initiated.

4.3 Design and production of Cylinders and Spheres with 3D Printer Technology

After the discussion of various materials such as wax and glass, and simulating lesion sizes, it was decided to use resin as the most robust and highly impermeable material in the printing process in the cleanroom facility of Boğaziçi University's Life Sciences and Technologies Application and Research Center (Boğaziçi LifeSci). The printing was carried out in a controlled room-temperature environment using a selected resin compatible with high-resolution 3D printers capable of processing biocompatible materials, with a layer thickness of 16 microns.

4.3.1 2-D Raw drawings of Spheres in Solidworks program

To prepare for printing, the initial raw drawings were created by determining the two-dimensional scale and dimensions using the SolidWorks program.

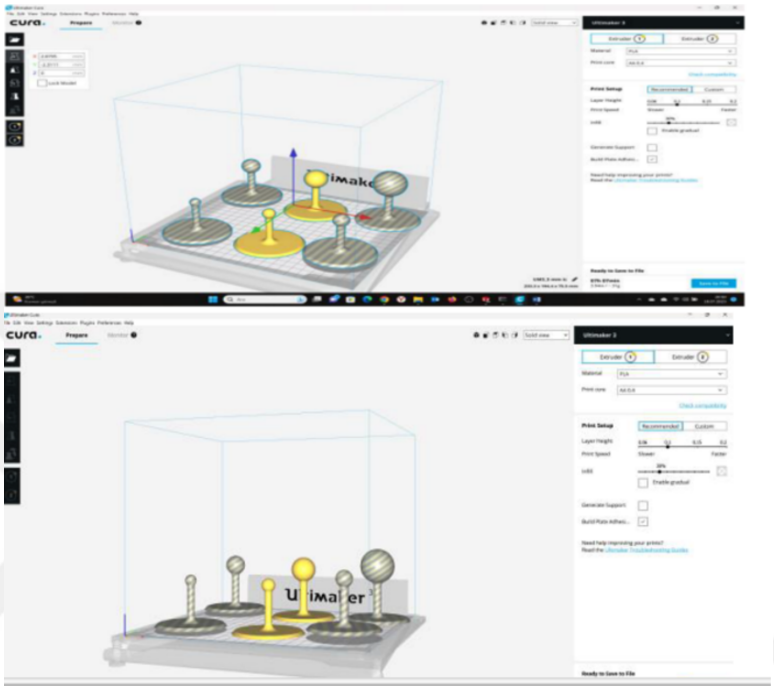


Figure 4.6 The solid models of the spheres.

The solid models of the spheres, whose two-dimensional drawings were created, making them ready for 3D printing (Figure 4.6).

Initially, various materials such as glass and wax were explored for the production of spheres to simulate lesion sizes. Following unsuccessful attempts, it was decided to employ resin, identified as the most robust material, and utilize 3D printing technology for its production.

For this purpose, for the initial trial prints, a black resin called "Vero Black" from the material palette shown in the Figure 4.7 below, which is compatible with the 3D printer's printing capability and available to us, was used.



Figure 4.7 "Vero black" out of 3D printer resin pallette.

4.3.2 3-D Printing of Spheres

After the transfer of the digital files of the designs to the 3D Printer was carried out, the spheres were ready to print. We defined 6 spheres with targeted diameters of 0.5 cm, 0.7 cm, 1 cm, 1.5 cm, 2 cm and 3 cm, representing lesion sizes. Using the 3D Printer Object Software program, we created solid model drawings with the ".stl" extension.

Converting the completed drawings of the samples into solid models has done for each 6 sizes of spheres separately. There are three sizes of big spheres (1.3 cm, 1.9 cm and 2.8 cm) and three sizes of small spheres (0.3 cm, 0.5 cm and 0.9 cm)

Subsequently, we printed them using the Object brand Connect 260 model 3D Printer located in Boğaziçi LifeSci's infrastructure as shown in Figure 4.8.



Figure 4.8 The first vero black - resin 3D printed prototypes.

Due to the narrowness of the channel through which we would inject the radioactive substance into the particles, we found that the support material generated during printing inside the particles could not be emptied and remained inside the particles. To remove the support material, we drilled the tip of each particle by 0.2 mm (200 microns) using a drill bit.

However, we observed that the drill bit we used to drill the interior surface of the smooth particles deformed the inner surface and caused burrs. At Bogazici University's Life Sciences and Technologies Application and Research Center (Boğaziçi Lifesci), specifically in the Pre-Clinical Laboratory equipped with a desktop CT device (MR Solutions), images were acquired and measurements were performed to verify the dimensions of the spheres as shown in the Figure 4.9 and Figure 4.10 below.

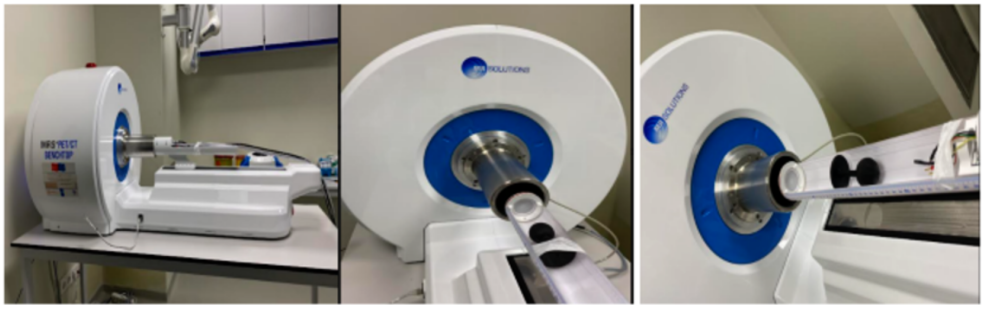


Figure 4.9 Boğaziçi Lifesci Pre-Clinic Lab. MR solutions desktop animal CT system.

As a result, in our study on black particles, we determined that the methodology of cleaning or emptying the support material inside the particles through drilling was

not suitable.



Figure 4.10 Boğaziçi Lifesci Pre-clinic Lab. MR solutions desktop animal CT system workstation.

After this study, it was determined that, due to their black color, the activity filling ratio inside the particles could not be fully observed in the initial water experiment, and efficient results could not be obtained. Therefore, it was decided to use transparent resin material and also to further reduce the lesion sizes. Planning and drawings were made, and new particles with diameters of 0.3 cm, 0.5 cm, 0.9 cm, 1.3 cm, 1.9 cm, and 2.8 cm were printed with transparent resin as shown in Figure 4.11.



Figure 4.11 Vero Clear - transparent resin and printed spheres.

At this stage, once again using the Object Connect 260 model 3D Printer in our center's infrastructure, we completed the printing of our spheres, this time using transparent 'Vero Clear' resin material as shown in Figure 4.12.

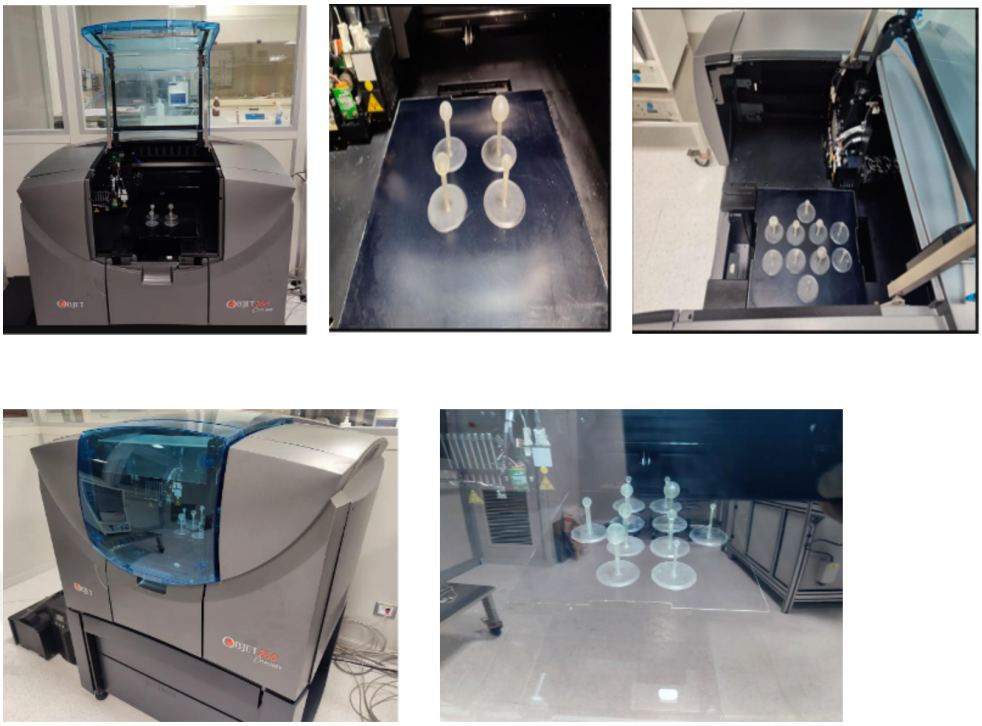


Figure 4.12 Object connect 260 model 3D printer and printed Veroclear-transparent spheres.

As for the method of removing the support material inside, we successfully cleaned it by injecting alcohol through the injection channel with a fine-tipped injector, without deforming the inner surface, which was originally opened for loading radioactive material. Subsequently, again in Boğaziçi LifeSci's pre-clinical laboratory, using Animal CT device from MR Solutions, a CT reference imaging of the spheres was performed (scout view), confirming that the surface remained undistorted as shown in Figure 4.13.

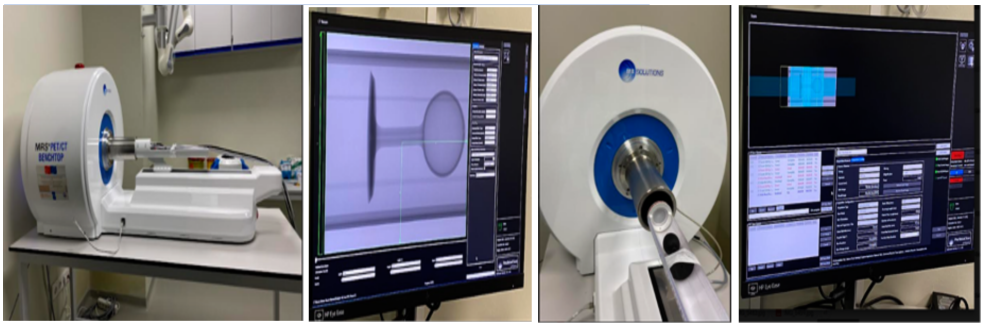


Figure 4.13 Lifesci Pre-Clinic Laboratory animal CT.

In addition, all spheres and cylinders were individually measured manually with a caliper device to confirm the accuracy of size measurements as shown in Figure 4.14.

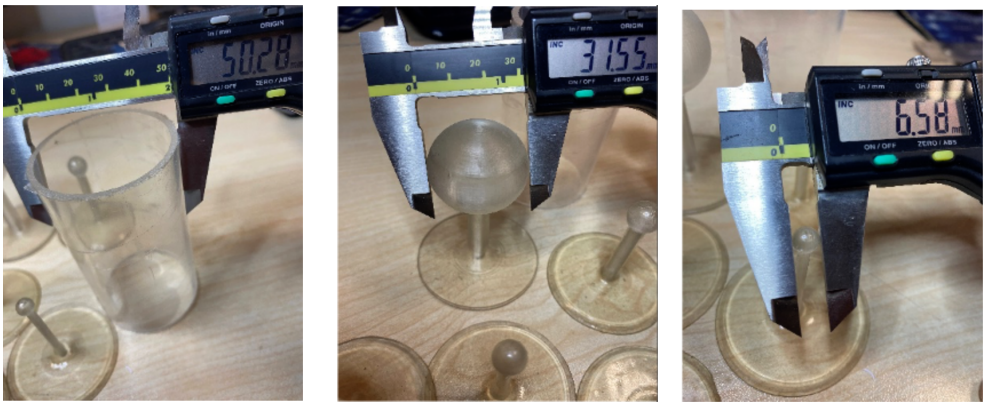


Figure 4.14 Caliper device size measurements.

After the entirety of the spheres was injected and prepared, for the verification of sphere dimensions, the CT of the General Electric brand Discovery NM-CT 670 model SPECT-CT System located in the Nuclear Medicine Clinic of Istanbul University, Istanbul Faculty of Medicine was utilized. Initially, the dimensions of black spheres were determined and verified, followed by the dimensions of transparently prepared vero clear resin spheres as shown in Figure 4.15. Subsequently, the spheres were prepared to assume their positions on the cylinders inside the Anthropomorphic phantom.



Figure 4.15 Istanbul University, Istanbul Faculty of Medicine, NM Department, size measurment of spheres under SPECT-CT.

4.3.3 3-D Raw Drawings and printing of cylinders

The necessary drawings and modeling to make the cylinders were prepared in SolidWorks (see Figure 4.16), and 6 cylinders were created by using plexiglass material.

Subsequently, the cutting works for the covers that would cover the top and bottom were carried out using the Epilog Laser Printer in our infrastructure (see Figure 4.17).

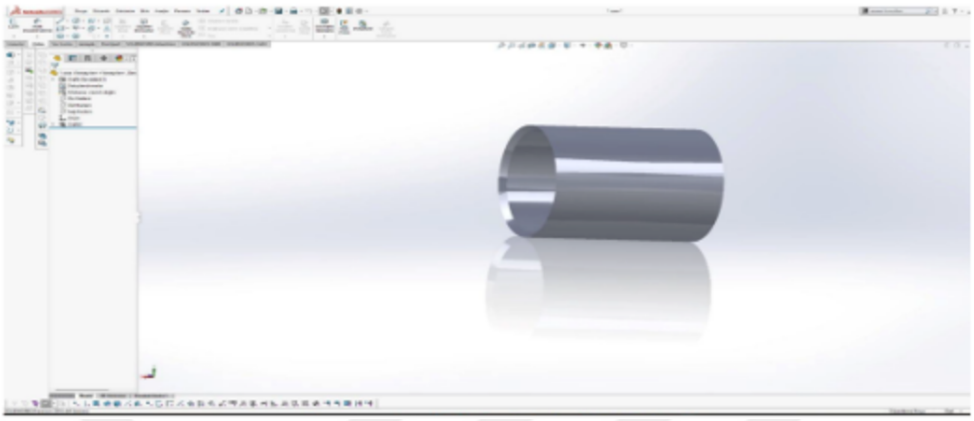


Figure 4.16 Design of outer cylinders.

After the Anthropomorphic phantom was ready, an inner space was created, where three plexiglass cylinders, each containing spheres simulating lesions of different sizes with a diameter of 5 cm, could simultaneously enter an adjacent cylindrical hole with a diameter of 5.4 cm. This hole was positioned to correspond to the Thorax, Abdomen, and Pelvic regions respectively.

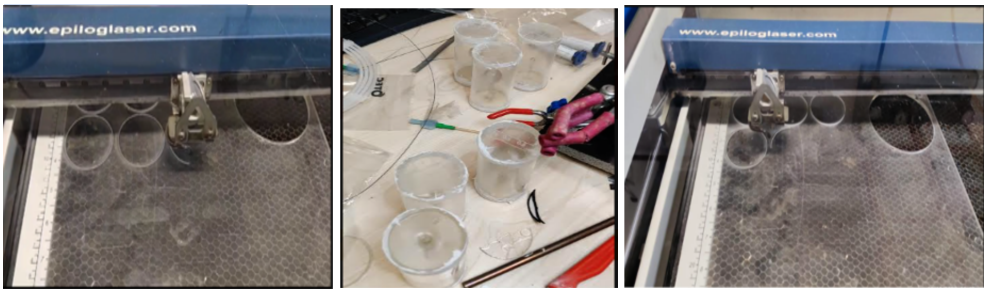


Figure 4.17 Printing of cylinders on Epilog laser printer.

A hole was drilled on the top of each cylinder for the injection of radioactive substance into the spheres, and a cover was created for each hole. Additionally, to observe the spill-in and spill-out effects, a hot background was prepared, and activities were planned to be placed inside the cylinder in ratios of 4:1 and 8:1. For this reason, a second hole was drilled on top of the cylinder, and a cover was made for it.

During the cylinder tests conducted with water in the Nuclear Medicine Clinic of Istanbul University, Istanbul Faculty of Medicine, it was identified that the air gap created during the injection of radioactive material into the spheres and the cylinder could lead to contamination by releasing back bubbles. Therefore, it was determined that a third hole should be drilled on top of the cylinder, and a separate cover should be made for it (see Figure 4.18).



Figure 4.18 Preparations of cylinders: (a) cylinders with 2 holes on top; (b) cylinders with 3 holes on top.

4.4 PET-CT System

Images were acquired with Analog and Digital PET-CT Technologies which are advanced medical imaging modalities used for diagnosing and staging various diseases, particularly cancer.

4.4.1 Analog PET-CT System

First three sites/hospitals had Analog PET-CT system which employs traditional photomultiplier tubes to detect gamma rays emitted by radiotracers, converting them into electrical signals for image generation.

4.4.2 Digital PET-CT System

The last site/hospital had Digital PET-CT system which utilizes solid-state detectors, such as silicon photomultipliers, to directly convert gamma rays into digital signals. In general, the digital approach offers advantages like improved sensitivity, spatial resolution, and quantitative accuracy compared to analog systems. Digital PET-CT technology has shown promise in enhancing diagnostic precision and enabling more personalized and targeted treatment strategies in the field of molecular imaging.

4.5 Hot Lab and Equipments

A Nuclear Medicine hot lab is an essential and specialized facility dedicated to the preparation of radiopharmaceuticals, handling radioactive materials, and conducting quality control. The equipment needed in an NM hot lab may differ depending on the specific activities and procedures.

In facilities handling radioactive materials, a variety of essential equipment and protective systems are employed to ensure operational safety, accuracy, and compliance with regulatory standards. A dose calibrator is utilized to measure and calibrate the activity of radioactive materials used in medical procedures. Gamma counters and well counters are applied to assess the radioactivity of samples such as blood or radiopharmaceutical preparations, ensuring accurate dosage administration. To maintain a safe working environment, fume hoods provide controlled conditions that minimize personnel exposure during the handling of radioactive substances. Additionally, glove boxes

offer enclosed workspaces equipped with integrated gloves, allowing the manipulation of radioactive materials while maintaining a physical barrier. Laminar flow hoods are used to facilitate the aseptic preparation of radiopharmaceuticals, reducing the risk of contamination during compounding processes. Lead-lined storage cabinets ensure the secure containment and shielding of radioactive materials. Radiation exposure among personnel is monitored through the use of personal dosimeters and area monitoring devices.

Moreover, quality control tools, including phantoms for imaging system validation, are employed to perform routine quality assurance checks. To minimize exposure during the preparation and administration of radioactive substances, syringe shields and vial shields are utilized. Radioactive waste generated during procedures is managed through appropriate waste disposal systems designed for safe containment. Furthermore, pH meters and sterility testing equipment are used to verify the chemical stability and microbiological safety of radiopharmaceuticals. Lastly, structural radiation shielding is implemented to provide a comprehensive protective environment for personnel against occupational radiation exposure.

4.6 FDG preperation and injection

The anthropomorphic phantom used in PET studies replicates human anatomy and is designed to mimic realistic conditions for imaging assessments. Key structures within the phantom, such as organs and tissues, are carefully crafted to simulate physiological characteristics, providing a controlled environment for evaluating imaging technologies.

Similar to clinical scenarios, FDG radiotracer production for anthropomorphic phantom studies involves the synthesis of fluorine-18 (18F) and its chemical incorporation into a glucose analog. Ensuring reproducibility and accuracy in radiotracer production is paramount to mimic realistic conditions and facilitate the translation of phantom study results to clinical practice.

4.7 Anthropomorphic Phantom Scans in Clinical Sites and Hospitals

In this thesis, we have studied in four different hospitals with four different PET-CT Systems and two different technology from three different vendors. The objective of this study was to conduct clinical scans by newly designed Anthropomorphic phantom on four distinct PET-CT systems, including the state-ofthe-art Digital PET-CT System featuring varied detector structures, introduced by different manufacturers and situated in diverse clinical centers. Calculating RCs for each system and technology to use in PVE correction. Detailed technical specifications of the PET-CT Systems and the hot labs where spheres were prepared (FDG injections applied) and PET-CT scans were performed and processing workstations are provided below respectively. ARPAT phantom prepared with cylinders and carried to sites as it is shown in the Figure 4.19.



Figure 4.19 (a)Arpat phantom and cylinders; (b) Spheres in cylinders; (c)Arpat phantom ready to carry on site.

4.7.1 Istanbul University, Istanbul Medical Faculty, NM Department - GE PET-CT System specifications

Site Equipment: GE Discovery IQ-4 PET-CT system (see Figure 4.20), Hot Lab equipments and processing workstations (see Figure 4.21, Figure 4.22). Furthermore, All PET/CT system specifications are given below (see Table 4.2).



Figure 4.20 Preparation of the ARPAT phantom prior to scanning and placement within the scanner.

Table 4.2
General Electric-GE Discovery IQ-4 PET-CT specifications

Technical Specifications	GE Discovery IQ-4 PET-CT System
Scanner Type	PET-CT
Detector Type	Bismuth Germanium Oxide (BGO)
Crystal size (mm)	6.3 x 6.3 x 30
CT Imaging	16-slice CT
PET Detector Rings	4 Rings
Spatial Resolution (PET)	<3 mm (transaxial) <3 mm (axial)
Slice Thickness (CT)	0.625 mm
Field of View (PET)	70 cm diameter
Maximum Patient Weight	Up to 500 lbs (227 kg)
PET Sensitivity	>90% (per NEMA NU2-2001 standards)
CT Spatial Resolution	<1 mm (high-resolution mode)
CT Dose Reduction Technologies	ASiR Veo
Image Reconstruction	Q.Clear ASiR-V
Image Display and Analysis SW	AW Server, AW Workstation
Power Requirements	200-240V, 50/60Hz, 32A
DICOM Compatibility	Yes
Radiation Dose Monitoring	Dose Check
Compliance	CE, FDA
Advanced Applications	Cardiac, Neurology, Oncology

Biodex Atomlab 500 Dose Calibrator and Hot- lab equipments: In this site, while injected FDG in our cylinders (for back ground) and spheres, we have used Atomlab 500 dose calibrator for dose calculations. Furtermore, there were all radiation

safety equipments as lead aprons, lead bricks, glows, surface meter etc. on site (see Figure 4.21).



Figure 4.21 Biodex Atomlab 500 dose calibrator and FDG preparation.

The Biodex Atomlab 500 is a dose calibrator designed for nuclear medicine and radiopharmacy. It ensures precise measurement and calibration of radioisotope activity. It accommodates a wide range of radionuclides, supporting quality assurance through calibration checks and the ability to draw doses directly from vials.



Figure 4.22 Workstation: GE Advantage Windows processing workstations.

4.7.2 Health Sciences University, Istanbul Training and Research Hospital, Nuclear Medicine Clinic - Siemens PET-CT System specificatons

Site Equipment: Siemens Biograph mCT 20 PET-CT System (see Figure 4.23) and Hot Lab equipments (see Figure 4.24) and processing workstations (see Figure

4.25). Furthermore, All PET/CT system specifications are given below (see Table 4.3).

Table 4.3
Siemens Biograph mCT 20 PET-CT system specifications.

Technical Specifications	Siemens Biograph mCT 20 PET-CT System
Scanner Type	PET-CT
Detector Type	Lutetium-based; Avalanche Photodiode (LSO)
Crystal size; mm	4 x 4 x 20
CT Imaging	20-slice CT
PET Detector Rings	4 Rings
Spatial Resolution (PET)	<4 mm (transaxial); <4 mm (axial)
Slice Thickness (CT)	0.33 - 1.0 mm
Field of View (PET)	78 cm diameter
Maximum Patient Weight	Up to 500 lbs (227 kg)
PET Sensitivity	>90% (per NEMA NU2-2007 standards)
CT Spatial Resolution	<0.5 mm (high-resolution mode)
CT Dose Reduction Technologies	CARE Dose; CARE kV
Image Reconstruction	TrueV; HD PET; UltraHD PET; SAFIRE
Image Display and Analysis Software	Syngo.via Acqusition Workplace
Power Requirements	200-240V; 50/60Hz; 32A
DICOM Compatibility	Yes
Radiation Dose Monitoring	Dose Check
Compliance	CE; FDA
Advanced Applications	Cardiovascular; Neurology; Oncology

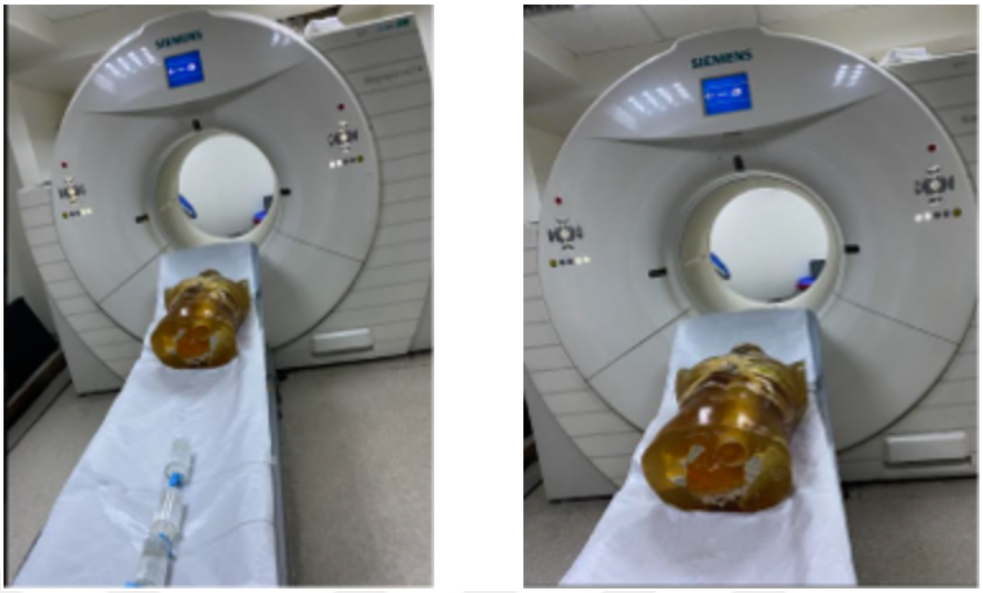


Figure 4.23 Arpat in PET-CT.

Biodex Atomlab100 Dose Calibrator and Hot- lab equipment: While injected FDG in our cylinders (for back ground) and spheres , we have used Atomlab100 dose calibrator for dose calculations. Furtermore, there were all radiation safety equipments as lead aprons, lead bricks, glows, surface meter etc. were ready on site.

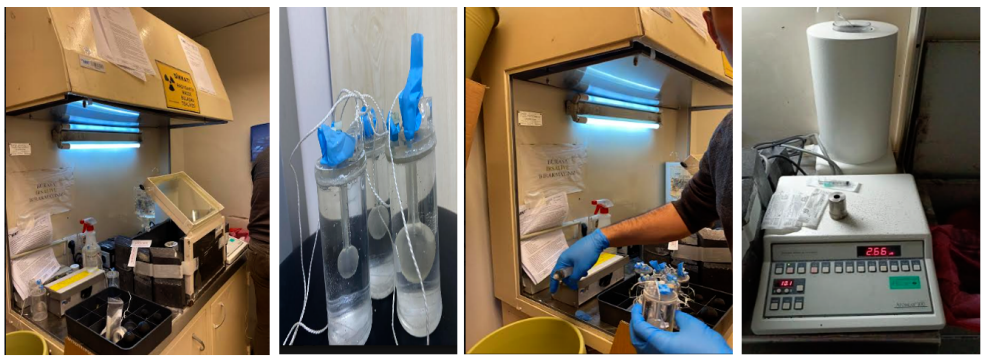


Figure 4.24 Biodex Atomlab dose calibrator.



Figure 4.25 Siemens Syngo acqusition workplace processing workstation.

4.7.3 Medipol University, Mega Hospital, Nuclear Medicine Department - Philips PET-CT System specificatons

Site Equipment: Philips GEMINI TF 16 PET-CT System (see Figure 4.26), Hot Lab equipments (see Figure 4.27) and processing workstations (see Figure 4.28). Furthermore, All PET/CT system specifications are given below (see Table 4.4).



Figure 4.26 Arpat is in Philips PET-CT.

Biodex Atomlab 500 Dose Calibrator and Hot-lab equipment: While injected FDG in our cylinders (for back ground) and spheres, we have used Atomlab 500 dose calibrator for dose calculations. Furtermore, there were all radiation safety equipments as lead aprons, lead bricks, glows, surface meter etc. were ready on site.

Table 4.4
Philips GEMINI TF 16 PET-CT system specifications.

Technical Specifications	Philips GEMINI TF 16 PET-CT System
Scanner Type	PET-CT
Detector Type	Lutetium-based, Avalanche Photodiode- LYSO
Crystal size, mm	4 x 4 x 22
CT Imaging	16-slice CT
PET Detector Rings	Dual-ring configuration
Spatial Resolution (PET)	<5 mm (transaxial), <5 mm (axial)
Slice Thickness (CT)	0.625 mm
Field of View (PET)	70 cm diameter
Maximum Patient Weight	Up to 450 lbs (204 kg)
PET Sensitivity	>90% (per NEMA NU2-2001 standards)
CT Spatial Resolution	<1 mm (high-resolution mode)
CT Dose Reduction Technologies	iDose, DoseRight
Image Reconstruction	Astonish, DoseRight
Image Display and Analysis SW	Extended Brilliance Workspace (EBW)
Power Requirements	200-240V, 50/60Hz, 32A
DICOM Compatibility	Yes
Radiation Dose Monitoring	DoseRight
Compliance	CE, FDA
Advanced Applications	Cardiovascular, Neurology, Oncology



Figure 4.27 FDG preperation and injection.

The Biodex Atomlab 500 is a dose calibrator designed for nuclear medicine and radiopharmacy. It ensures precise measurement and calibration of radioisotope activity. With an intuitive interface, it accommodates a wide range of radionuclides,

supporting quality assurance through calibration checks and the ability to draw doses directly from vials.

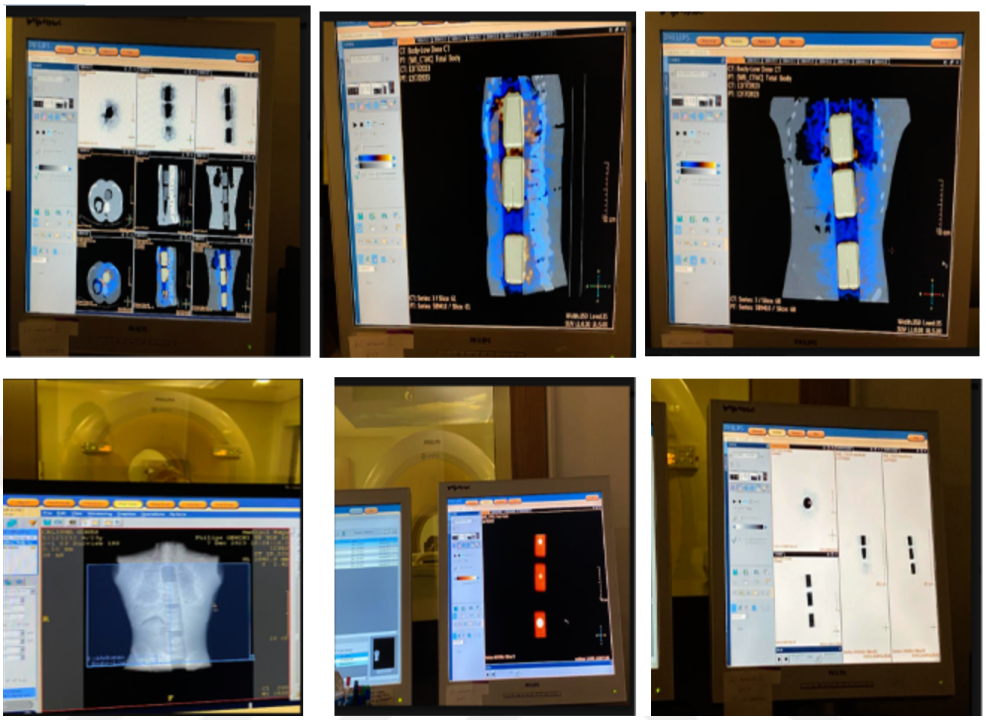


Figure 4.28 Extended Brilliance Workspace (EBW) processing workstation.

4.7.4 Prof. Dr. Cemil Taşçıoğlu City Hospital, Health Application and Research Center, Nuclear Medicine Clinic - GE Digital PET-CT System specificatons

System specificatons Site Equipment: GE Discovery MI Digital PET-CT System (see Figure 4.29), Hot Lab equipments (see Figure 4.30), and processing workstations (see Figure 4.31). Furthermore, All PET/CT system specifications are given below (see Table 4.5).

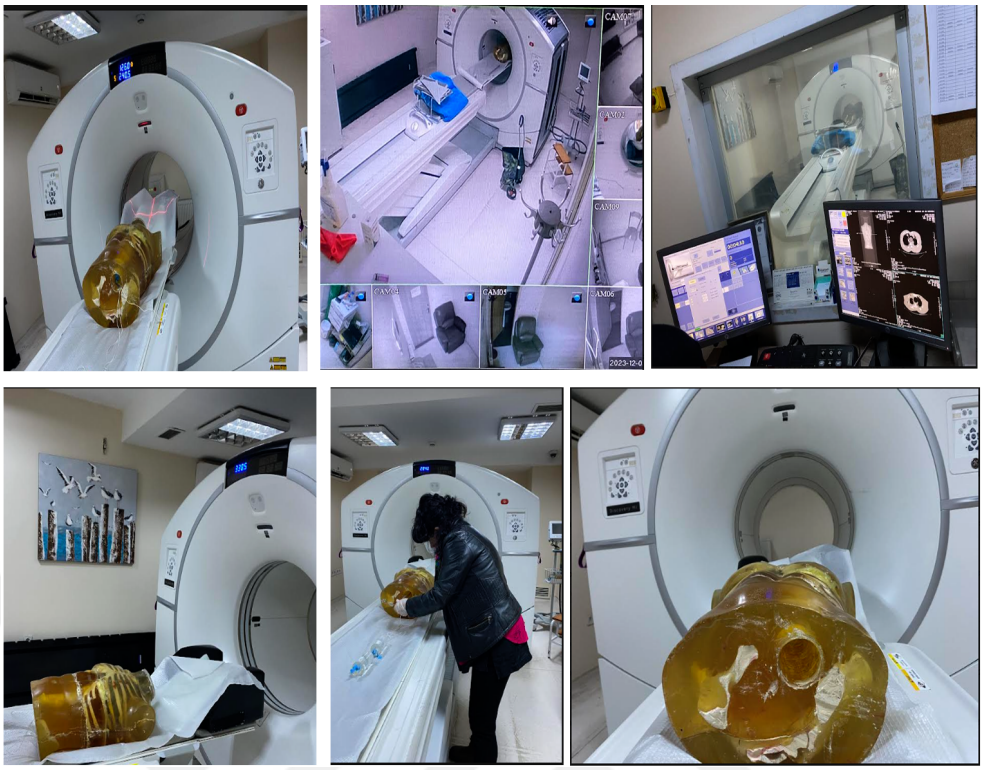


Figure 4.29 Arpat in digital PET-CT.

While injected FDG in our cylinders (for back ground) and spheres, we have used Biodex Atomlab 500 dose calibrator for dose calculations as in previous site. Furtermore, there were all radiation safety equipments as lead aprons, lead bricks, glows, surface meter etc. were ready on site.

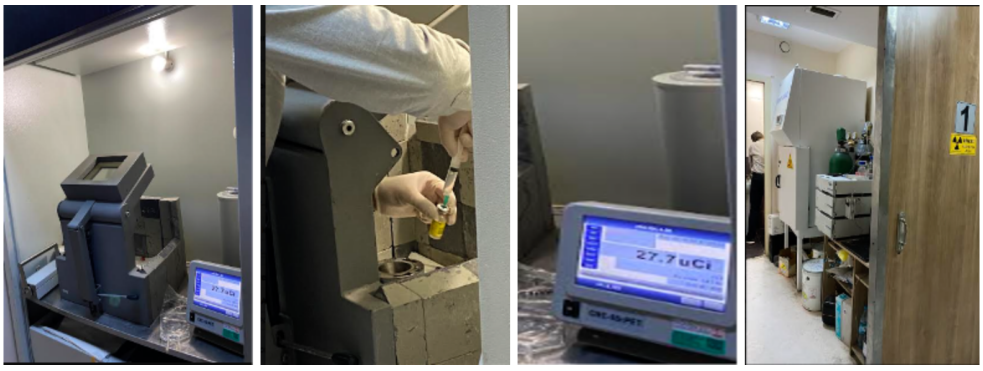


Figure 4.30 FDG preperation and injection.

All post processings have done on GE's Advantage Windows workstations.

Table 4.5
GE Discovery MI Digital PET-CT system specifications.

Technical Specifications	GE Discovery MI Digital PET-CT
Scanner Type	PET-CT
Detector Type	Silicon Photomultiplier (SiPM), LYSO
Crystal size, mm	3.95 x 5.3 x 25
CT Imaging	128-slice CT
PET Detector Rings	Multiple, configurable
Spatial Resolution (PET)	4 mm (transaxial), <4 mm (axial)
Slice Thickness (CT)	0.625 mm
Field of View (PET)	70 cm diameter
Maximum Patient Weight	Up to 500 lbs (227 kg)
PET Sensitivity	>90% (per NEMA NU2-2018 standards)
CT Spatial Resolution	<0.5 mm (high-resolution mode)
CT Dose Reduction Technologies	ASiR, Veo
Image Reconstruction	Q.Clear, ASiR-V
Image Display and Analysis SW	AW Server, AW Workstation
Power Requirements	200-240V, 50/60Hz, 32A
DICOM Compatibility	Yes
Radiation Dose Monitoring	Dose Check
Compliance	CE, FDA
Advanced Applications	Cardiac, Neurology, Oncology

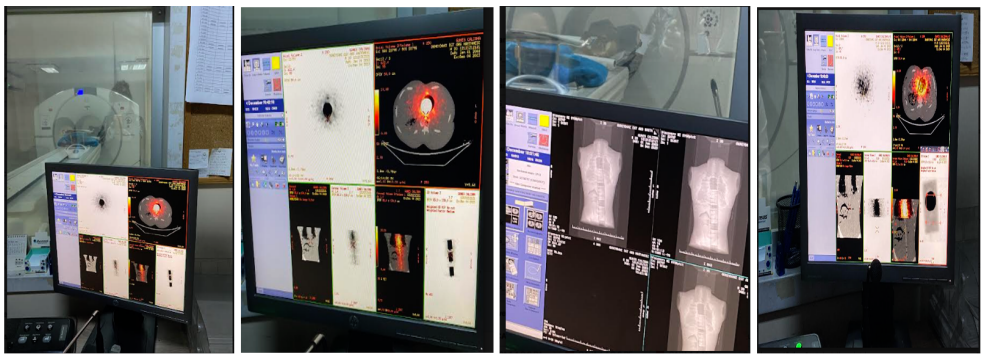


Figure 4.31 Advantage Windows processing workstation.

4.8 Scan parameters and injected radioactivity dose (FDG) to spheres and to cylinders for Back Ground (BG) activities

Although the PET-CT systems and technologies differed among the hospitals (with the technical specifications detailed in Chapter 4.7), imaging procedures were performed following identical standard conditions and protocols at all sites as shown in the Table 4.6 below.

Table 4.6
Scan parameters.

PET Scan	Static Whole Body PET
CT Scan	Static Whole Body CT
Scan Time	2 minutes per bed position
Number of beds	Changes system to system according to FOV

The FDG (Fluorodeoxyglucose) dose, for each hospital, was diluted in saline solution at the same time for all rates, and injected in equal ratios into all cylinders and spheres under the conditions specified in the Table 4.7 below.

Table 4.7
Dose parameters.

	Saline Solution	Injected Ratio	Injected dose (FDG)
Cylinders (Back Ground)	1000 ml	1	2 mili Curi
Spheres 4:1	250 ml	4	2 mili Curi
Spheres 8:1	125 ml	8	2 mili Curi

There were 6 cylinders in the same sizes and 6 spheres positioned in these cylinders which have different sizes and simulate the lesions with diameters of 0.3, 0.5, 0.9, 1.3, 1.9 and 2.8 cm respectively as shown in the Figure 4.32.



Figure 4.32 Cylinders for reference scan.

The cylinders and spheres in Anthropomorphic Phantom were prepared using F18-FDG solutions. The cylinders was filled with activity concentration 2 mci background uptake maintained consistently throughout all scans. Each sphere was initially infused with a particular concentration of activity 8 times higher than the back ground concentration. It corresponds to sphere to back ground ratio (n) of n=8:1. Then, the study was repeated for n=4:1.

The activity levels of the FDG solutions injected in the spheres and cylinders (inserted in the Anthropomorphic phantom) were measured using the dose calibrators which were mentioned in each site's hot lab equipment specifications separately.

4.9 Image acqusition, reconstruction and quantification

The first sequence of image acqusition was performed by Anthropomorphic phantom. 3 sets of cylinders which include spheres in sizes 0.3, 0.5 and 0.9 cm (small spheres) have scanned simultaneously in order Thorax- Abdomen and Pelvic regions respectively. Scans repeated by changing the order of all spheres till all sizes have seperately scanned for Thorax-Abdomen and Pelvic images.

Then, the same procedure has repeated for the other 3 cylinders which include spheres in sizes 1.3, 1.9 and 2.8 (big spheres) respectively.

The acquisitions were repeated for cylinders (including spheres in) without the Anthropoformic Phantom to get scatter free images out of body attenuation as a reference image for each site.

TThe images were acquired in each site separately and reconstructed following the clinical guidelines applied oncological studies at these sites. In each acquisition, different number of bed positions has taken by depending on the specifications of FOV for each system in different sites but each bed position (has taken 2 minutes) positioned in the plane that passes through the center of the spheres. The attenuation correction was performed by CT scan.

Different reconstruction algorithms were applied to reconstruct the PET images, utilizing various matrix sizes based on the specifications of the PET-CT systems at different sites, as outlined above.

Reconstructed image evaluations have performed in Yeditepe University, GE's

Advantage Windows workstations. During the image quantification, the slice that aligned with the center of the spheres in each scan was selected. The peak activity concentration in the spheres was quantified by manually defining circular Volumes of Interest (VOIs) on each sphere's image, separately for each region (thorax, abdomen, pelvis), each scanning site, and for the spheres excluding the phantom (reference image – scatter-free). The VOIs on the PET images were positioned based on anatomical details obtained from the corresponding CT images.

Based on the activity concentration values measured in all the spheres and the background region, the RC for each sphere was calculated for 4:1 and 8:1 ratios and reference images (scatter free-without phantom) separately by using the equation as below Eq. 4.1.

$$RC = \frac{MeasuredActivityConc.(Sphere) - MeasuredActivityConc.(Background)}{KnownActivityConc.(Sphere) - KnownActivityConc.(Background)} \tag{4.1}$$

In this equation, Measured Activity Concentration (Sphere) refers to the measured activity concentration within the sphere, while Measured Activity Concentration (Background) represents the measured activity concentration in the background. Known Activity Concentration (Sphere) denotes the known or true activity concentration in the sphere, and Known Activity Concentration (Background) refers to the known or true activity concentration in the background.

"Activity decay" is calculated for each sphere groups and taken into consideration for RC calculations for n=4:1, n=8:1 ratios and reference images separately for each sites.

The RCs (Recovery Coefficients) reflect the scanner's capability to precisely measure activity concentration values within the spheres. These coefficients, which lack units, are ideally situated on a scale from 0 to 1. A RC of 0 suggests that the

scanner cannot measure the activity concentration in the sphere, while an RC of 1 signifies a measurement equivalent to 100% of the known concentration.

5. RESULTS

Sphere and background activities are measured in each site with six different sizes of spheres (0.3, 0.5, 0.9, 1.3, 1.9 and 2.8 cm) on 4:1 and 8:1 ratio and for each three anatomical regions (thorax, abdomen, pelvis). Accordingly, RC values are calculated for each sphere. While doing all these calculations, according to F-18 FDG injected time, to eliminate half time effect, activity decay calculations taken into consideration to get more realistic results. The calculated RCs are shown in Tables 5.1 - 5.4 for each site separately.

The RCs measure how well the imaging system recovers the true activity concentration within a region of interest (ROI), such as a lesion or a tumor.

After doing all calculations, RC data was analyzed and fitted to the Asymptotic Regression Model function with the following Eq. 5.1.

$$Y = a - bc^x \tag{5.1}$$

Table 5.1
For acquisitions at n=4:1 and n=8:1, RC values for each anatomical region and each sphere for site-1.

Sphere(cm)	4:1 Thorax	4:1 Abdomen	4:1 Pelvis	8:1 Thorax	8:1 Abdomen	8:1 Pelvis
0.3	0.122	0.133	0.154	0.075	0.048	0.086
0.5	0.372	0.313	0.297	0.097	0.089	0.075
0.9	0.425	0.478	0.473	0.36	0.347	0.306
1.3	0.616	0.5	0.555	0.379	0.361	0.392
1.9	0.629	0.671	0.592	0.556	0.491	0.451
2.8	0.677	0.714	0.799	0.59	0.744	0.624

The software facilitated precise curve fitting and data analysis, enabling a thorough examination of the RC characteristics. The utilization of the Asymptotic Regres-

Table 5.2
For acquisitions at n=4:1 and n=8:1, RC values for each anatomical region and each sphere for site-2.

Sphere(cm)	4:1 Thorax	4:1 Abdomen	4:1 Pelvis	8:1 Thorax	8:1 Abdomen	8:1 Pelvis
0.3	0.11	0.133	0.115	0.115	0.093	0.152
0.5	0.251	0.218	0.262	0.243	0.217	0.228
0.9	0.43	0.404	0.421	0.295	0.305	0.291
1.3	0.549	0.549	0.527	0.581	0.606	0.564
1.9	0.648	0.679	0.635	0.717	0.645	0.615
2.8	0.767	0.847	0.819	0.878	0.815	0.871

Table 5.3
For acquisitions at n=4:1 and n=8:1, RC values for each anatomical region and each sphere for site-3.

Sphere(cm)	4:1 Thorax	4:1 Abdomen	4:1 Pelvis	8:1 Thorax	8:1 Abdomen	8:1 Pelvis
0.3	0.085	0.116	0.116	0.118	0.107	0.1
0.5	0.135	0.198	0.116	0.212	0.239	0.187
0.9	0.307	0.336	0.29	0.406	0.349	0.397
1.3	0.533	0.53	0.637	0.47	0.507	0.514
1.9	0.745	0.805	0.704	0.494	0.552	0.534
2.8	0.862	0.812	0.818	0.821	0.75	0.746

sion Model provided a robust framework for understanding the asymptotic behavior of the data. This approach ensured the reliability and accuracy of the results (RCs) when comparing clinical data, allowing for a deeper insight into the underlying trends and patterns.

Table 5.4
For acquisitions at n=4:1 and n=8:1, RC values for each anatomical region and each sphere for site-4.

Sphere(cm)	4:1 Thorax	4:1 Abdomen	4:1 Pelvis	8:1 Thorax	8:1 Abdomen	8:1 Pelvis
0.3	0.087	0.129	0.124	0.112	0.102	0.118
0.5	0.186	0.211	0.182	0.227	0.202	0.192
0.9	0.476	0.407	0.423	0.336	0.305	0.335
1.3	0.497	0.517	0.567	0.467	0.439	0.405
1.9	0.623	0.671	0.668	0.6	0.517	0.534
2.8	0.782	0.738	0.768	0.74	0.726	0.706

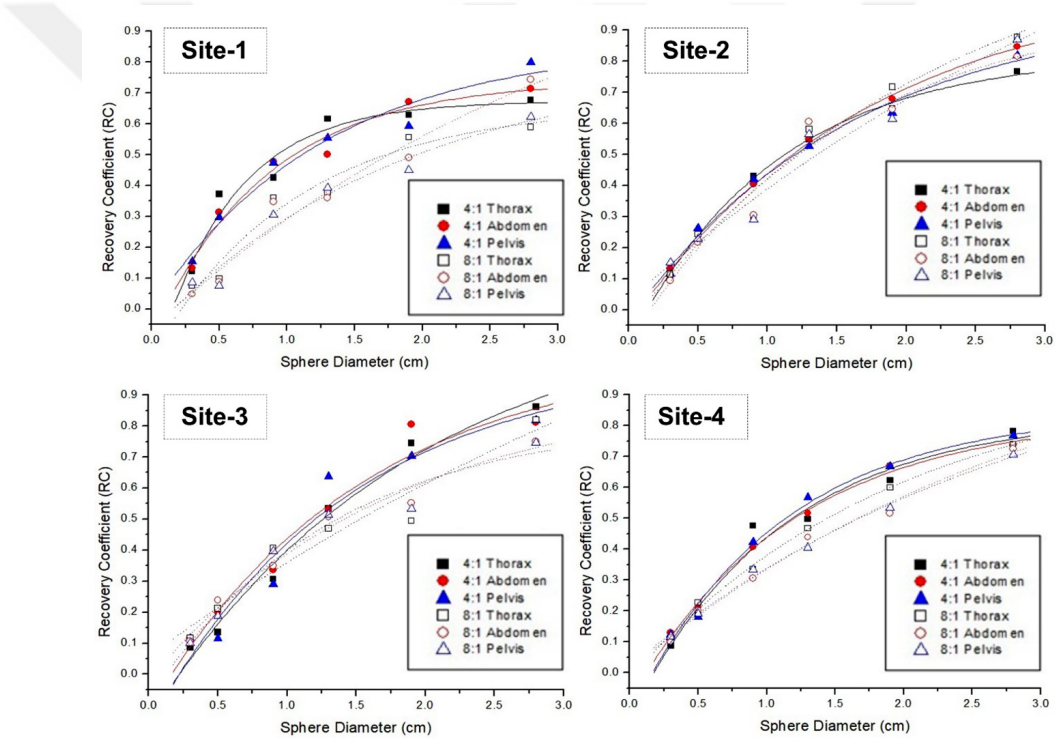


Figure 5.1 Recovery coefficients as a function of the diameter of spheres for all sites.

Figures 5.2-5.4 show respectively for each site; the curves generated from RCs as a function of the sphere diameters, for 3 anatomical regions for n=4:1 and n=8:1 for all sites.

We analyzed the relationship between sphere diameter and recovery coefficient (RC) as depicted in the graph. The x-axis represents the sphere diameter used in the

study, ranging from very small diameters (a few millimeters) to larger ones (several centimeters), while the y-axis represents the RCs, typically ranging from 0 to 1. An RC of 1 indicates perfect recovery, where the measured activity equals the true activity, whereas an RC less than 1 indicates underestimation. The graph typically shows that for small spheres, the RC is low due to partial volume effects, where the imaging system struggles to capture the true activity concentration accurately. As the sphere diameter increases, the RC generally increases because larger objects are better resolved by the imaging system, leading to more accurate activity measurements. Eventually, the RC may plateau and approach 1 for larger spheres, indicating that the imaging system can accurately recover the true activity concentration for these objects. Additionally, the spatial resolution of the imaging system plays a crucial role, with higher resolution systems yielding better RCs for smaller diameters.

When plotting RCs against the diameters of spheres, the graph typically shows how well the imaging system can recover the true activity concentration for objects of different sizes. To observe how the RCs varied with tumor sizes (spheres) in the thorax, abdomen, and pelvis regions for each "n" value (n=4:1 and n=8:1) at 4 different sites, relevant graphs were generated. These graphs provided a visual representation of the RC's dependency on tumor dimensions, offering insights into the quantitative relationships across different anatomical regions and varying "n" values.

Figures 5.2, 5.3 and 5.4, show respectively; the curves generated from RCs as a function of the sphere diameters, for 3 anatomical regions for n=4:1 and n=8:1 for all sites.

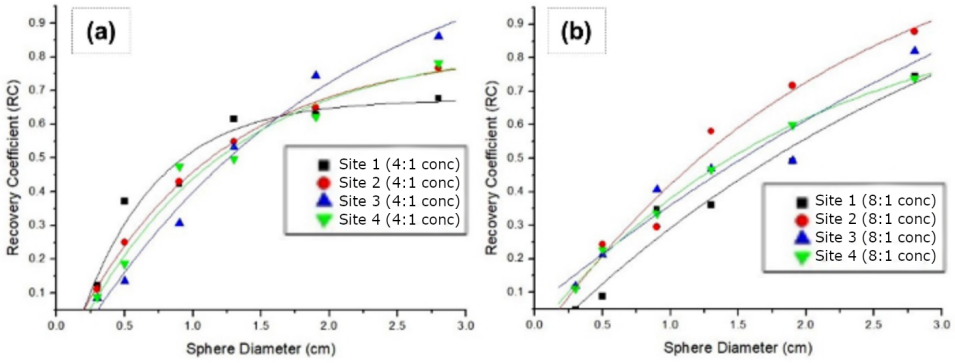


Figure 5.2 Variation of RCs with tumor sizes (spheres) in the thorax region for n values (a) n=4:1 and (b) n=8:1 for all four sites.

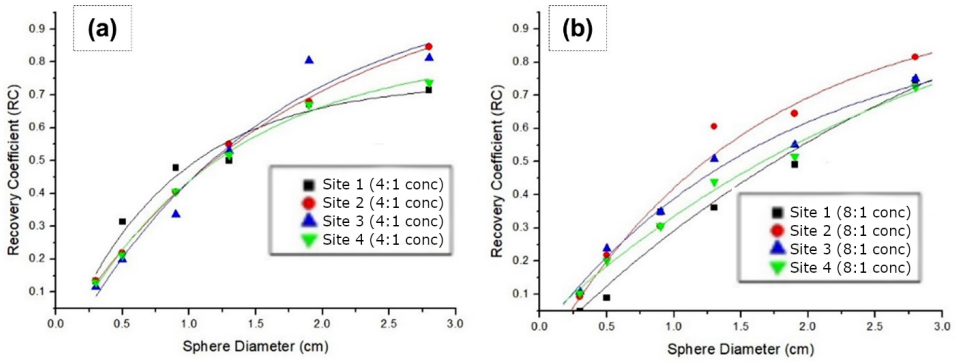


Figure 5.3 Variation of RCs with tumor sizes (spheres) in the abdomen region for n values (a) n=4:1 and (b) n=8:1 for all four sites.

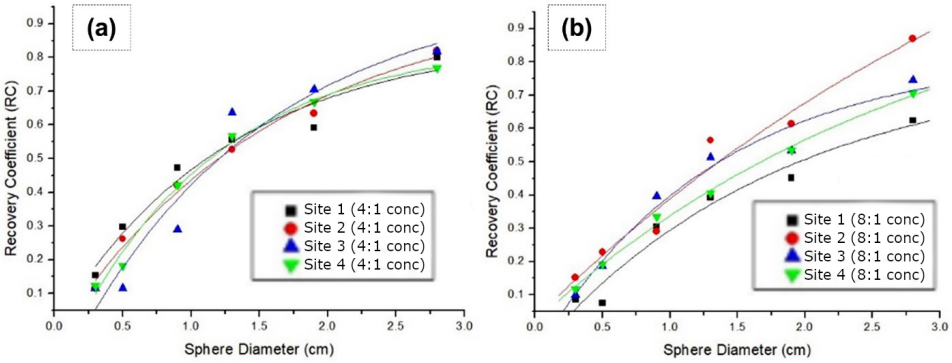


Figure 5.4 Variation of RCs with tumor sizes (spheres) in the pelvis region for n values (a) n=4:1 and (b) n=8:1 for all four sites.

6. DISCUSSION

Accurate SUV measurements are vital for many tumors where metabolic activity measurement allows for the assessment of treatment response. Correcting the uptake obtained from the patient with RC can help to eliminate measurement discrepancies between devices.

Anthropomorphic phantoms with known properties and corrected SUV values can assist in calibrating PET scanners, ensuring that the equipment is functioning correctly and producing reliable data [7, 40].

The utilization of SUV corrected values with phantom imaging is vital for maintaining the accuracy, consistency, and standardization of PET imaging. These values are integral to quality control, equipment calibration, research, clinical decision-making, and collaborative studies across multiple centers. Employing these standardized measures allows clinicians and researchers to obtain precise and comparable data from PET imaging, which in turn enhances patient outcomes and drives progress in medical imaging technology [40].

One significant reason for inaccurate SUV measurement is the small size of the lesion, which often results in measurements being lower than expected. As the diameter of the sphere (or tumor) decreases, the impact of the Partial Volume Effect (PVE) becomes more pronounced. This situation highlights how scatter radiation outside the FOV (Field of View) significantly reduces counts in smaller-diameter regions by increasing the dead time of the detection system [30]. Conversely, for larger spheres, the influence of PVE is less pronounced, and scatter radiation outside the FOV does not significantly reduce counts in these regions. These findings are consistent with studies by Matheoud et al. and Krempser et al., and our results are similar [2, 41].

In PET and SPECT imaging, it is essential to account for and incorporate

activity outside the FOV when calculating RCs to improve the accuracy of RC-based PVE correction methods. This approach is particularly crucial as it addresses the influence of scattered radiation and spill-over effects, leading to a more comprehensive correction methodology [41].

In the clinical setting, estimating scatter from outside the FOV is challenging. Nevertheless, using anthropomorphic phantoms proves to be a valuable strategy for optimizing the determination of RC in clinical acquisitions [37].

Analysis of this study's results, consistent with Krempser et al.'s investigation [2], indicates that the variability in sphere diameter among RCs is more pronounced than the variability related to the n value. Notably, RCs exhibit significant variation as the sphere diameter ranges from 0.3 cm to 0.9 cm. This observation is critical as it demonstrates that smaller spheres are more susceptible to variability, which must be accounted for in quantitative analyses. Furthermore, all RC curves tend to stabilize at the unit value of 1, indicating that the measured activity concentration equals the known activity concentration as the sphere diameter increases from 0.3 cm to 2.8 cm. This stabilization highlights a threshold beyond which further increases in sphere diameter do not significantly impact RCs, simplifying the interpretation of results for larger spheres.

Additionally, it was observed that RCs increase with higher n values, indicating a correlation between these n values and RC stability. This relationship enhances our understanding of how sphere diameter, n values, and RCs interact, offering valuable insights into the complexities of partial volume effects (PVE) in PET imaging. This nuanced understanding can improve the accuracy of PET imaging by better accounting for PVE, leading to more reliable quantification of metabolic activity in clinical settings. By acknowledging and incorporating these factors, we believe it would be possible to improve the accuracy of quantitative PET analyses, leading to more reliable and interpretable data. This understanding underscores the importance of considering both sphere diameter and n values when designing and interpreting PET studies to mitigate the impact of PVE and enhance the overall robustness of imaging results.

In our study involving the unique anthropomorphic phantom, the primary aim was not to compare the RC values with those obtained from the NEMA gold standard phantom, due to differences in spherical sizes and phantom characteristics. However, upon reviewing reference studies that utilized the NEMA phantom, it was observed that all of its spherical lesion sizes exceed 1 cm. Notably, the 1.3 cm and 2.8 cm lesion sizes from both phantoms can be directly compared.

In our study, RC determined reached up to 0.9 (equivalent to 90% of recovery counts) for sphere diameters of 2.8 cm with Anthropomorphic fantom studies. In contrast, Srinivas et al reported RCs up to 0.8, and Krempser et al achieved up to 1 in their investigations with PET-NEMA phantoms in 1:8 ratio. Furthermore, when examining the 1.3 cm lesion size in both reference studies, we observed that the RC values differed significantly. In Srinivas' study, the RC value was 0.25, while in Krempser's study it was 0.65. In contrast, our study yielded an RC value of 0.6 for the same lesion size. These discrepancies may be attributed to differences in phantom characteristics, imaging techniques, or other experimental factors [2, 31].

RCs exhibit a notable specificity based on the unique characteristics of a given scanner and the specific radiopharmaceuticals used. Consequently, they cannot be universally applied for PVE correction across different scanners or for images obtained with the same scanner but using a radiopharmaceutical other than F18-FDG, as emphasized by Gallivanone et al. [4].

In our study, we extended the experimental replication to assess RCs, considering scanners even from the same manufacturer (Site 1 and Site 4) but of different models. This approach was motivated by the recognition of the distinct influence exerted by each detection system and the parameters of image reconstruction algorithms. The findings underscore the need for a tailored and scanner-specific approach when addressing PVE in quantitative analyses, taking into account both the technological specifications and reconstruction algorithms of the imaging systems employed [26, 27, 42]. This consideration becomes particularly relevant in multi-site or multi-model studies where harmonizing RCs across different systems is essential for accurate

and consistent quantitative assessments.

We observed variability in RCs across different PET/CT systems in different detector Technologies (digital SiPM, Silicon Photo Multiplier, vs analog PMT, Photo Multiplier Tube), driven by key factors. Detector technology plays a major role in sensitivity and temporal resolution. TOF (Time of Flight) technology, reduces noise and enhances spatial resolution, while non-TOF systems may struggle with accuracy. Variations in reconstruction algorithms (e.g. GE's Q.Clear, Siemens' HD-PET), axial field of view, system sensitivity, and equipment age or maintenance of the equipment also contribute to the observed differences.

We obtained RC values for 6 different sizes in three regions: Thorax, abdomen, and pelvis. These RC values have allowed us to standardize the mean SUV values of tumors of equivalent sizes obtained from real clinical patients, making them independent of factors related to the device and patient attenuation. This enables the elimination of differences in uptake values obtained using different devices, particularly during patient follow-up, providing the opportunity for accurate comparison and interpretation of PET results conducted at different centers.

Krempser et al. stated in their study [2] that as the n values increase, the RC also increases. However, in the study conducted at Site-1, it was observed that the RC values decreased. This discrepancy is thought to be due to the time differences between the loading of activity and the initiation of imaging.

In delayed imaging, as the activity count within the phantom decreases, the noise in the images increases, leading to greater uncertainty in the measurements. This rise in noise levels can significantly affect the accuracy and precision of the recovery coefficient (RC) values, potentially skewing the results. The increased uncertainty might be attributed to the diminished signal-to-noise ratio (SNR), which poses a challenge in accurately quantifying the RC, especially in lower activity regions. Future studies should consider optimizing the timing of activity loading and imaging initiation to mitigate these effects and ensure more reliable and consistent RC measurements.

As observed from the graphs generated in this study, it is evident that the RC values measured in the thorax, abdomen, and pelvis are similar across all centers. This result indicates that the RC values do not vary significantly with the position of the body. The consistency of RC values across different anatomical regions suggests that the recovery coefficient is not influenced by the specific location within the body. This finding is important as it underscores the robustness of the RC as a parameter, implying that it can be reliably used for quantitative assessments regardless of the anatomical region being imaged. Such uniformity enhances the utility of RC measurements in clinical and research settings, ensuring that comparisons and interpretations of RC data are valid and not confounded by positional differences. Further studies could expand on this by exploring other potential factors that might affect RC values, thereby providing a more comprehensive understanding of the parameters influencing RC measurements.

Gallivanone et al. applied the statistical t-test to obtain p-values for comparing lesion sizes and SUV values in oncological patient groups [4]. Similarly, Bettinardi et al., in their review article, highlighted the statistical significance of correlations between PET biomarkers and biological prognostic indices or survival endpoints [7]. Furthermore, Koopman et al. also employed the t-test in their statistical analysis to compare patient and scan characteristics between two scanning groups, using p-values for these comparisons [26]. In this study, p-values were calculated using linear regression analysis; where the RC values calculated at different sites for all three anatomical regions and both n (1:4, 1:8) ratios were processed.

Two separate linear regression models were applied using R: A Language and Environment for Statistical Computing to evaluate the impact of various factors on the dependent variable (RC).

First model involves all parameters and considers direct effects only. Results of this first model, parallel to our study, demonstrate that while region does not appear to influence the dependent variable ($p>0.1$), Site-2 ($p<0.001$) and Site-3 ($0.01<p<0.1$) do have a statistically significant impact.

Second model was employed to understand combined effect of sphere size and sites, where region parameter was removed. The results from this second model confirms combined effect of sphere size and Site-2 ($0.001<p<0.01$) and Site-3 ($0.001<p<0.01$) has statistically significant effect. These results also show effect of site increases with increasing sphere size, as all direct site parameters have $p>0.1$.

Analyzing the pixel sizes of the PET/CT systems at each center reveals that, for a system with a resolution of 5 mm and a pixel size of 4 mm, placing a 3 mm sphere simulating a lesion for measurement illustrates the challenges of detecting activity uptake in small-scale lesions. Although the activity uptake in these small spheres can be detected, the results are not statistically significant.

This finding underscores the limitations of current PET/CT technology in accurately quantifying RC values for very small lesions. The discrepancy likely arises due to the resolution constraints, where the partial volume effect becomes more pronounced, and the activity distribution within such small volumes is not accurately captured. Consequently, this leads to increased uncertainty and variability in the measured RC values, making them unreliable for clinical or research applications in small lesions.

These limitations highlight the need for advancements in imaging technology to improve spatial resolution, detector sensitivity and reduce pixel size, thereby enabling more accurate detection and quantification of activity in smaller lesions. Future research should focus on developing enhanced imaging techniques and algorithms that can better account for these limitations, potentially incorporating high-resolution imaging systems or advanced image reconstruction methods to achieve more reliable results in small-scale lesion measurements.

As indicated above, in all devices, the obtained RC value for 0.3 cm is quite low. The highest value is achieved for the Thorax region at Site-1, while the lowest results obtained at Sites 3 and 4 are close to each other. Across centers, as the lesion size increases, the RC values approach each other. Therefore, the sphere simulating the lesion, with a size of 0.3 cm, is below the resolution limit for all devices, and semi-

quantitative values obtained from lesions of this size are not reliable for diagnosis and follow up treatment response.

At Site 4, where the Digital PET/CT system is located, although the image quality is very high, and lesion detection is at an advanced level (since system has TOF- Time of Flight and Q-Clear as well), the low RC values compared to other sites (even in large spheres, around 0.7, 0.8 ratios) may indicate a potential error in SUV calibration. For each device and each size, RCs have been obtained that will enable the standardization of quantitative values. Our results indicate that similar studies could contribute to the assessment of patients in the future, especially the ones with small tumors. A larger scale chart study needs to be conducted to provide a more extensive dataset for all targeted tumor sizes using similar specialized anthromorphic phantoms and the methodology described in this study.

7. CONCLUSION

This study is pioneering as it marks the first application of an anthropomorphic phantom in lesions smaller than 1 cm (0.3, 0.5, 0.9) in molecular imaging. A primary objective for future research is to develop phantoms that simulate various life stages—such as pediatric, adolescent, adult, and elderly patient groups—along with different body volumes. Ultimately, our aim is to create a virtual phantom using AI-supported software to enhance and standardize quantitative data across patient groups by utilizing recovery coefficient (RC) values derived from these phantoms.

In this preliminary study, we believe we have reached significant initial results to determine the RC values necessary for accurately measuring the tumoral radiopharmaceutical uptake in patients.

There are two main reasons for determining corrected SUV values. The first reason is that it allows for the development of a perspective to correct the significant numerical discrepancies caused by different PET/CT systems operating worldwide. This correction will guide clinicians on the percentage changes in SUV to consider, particularly regarding treatment response. The second reason is that it will enable the use of corrected SUV parameters, independent of the device, in algorithms and evaluations used in the rapidly proliferating artificial intelligence applications, facilitating their use in patient assessments in a much shorter time.

The standardization of PET imaging results is a fundamental requirement for the accurate evaluation of molecular imaging outcomes. Therefore, we believe that the RC values derived from the results of our study using the first prototype of the anthropomorphic phantom, which we consider to be the most realistic, could significantly contribute to the increased confidence in the numerical results obtained from molecular imaging in the coming years. However, there is still a need for the development of more realistic anthropomorphic phantoms and the use of these phantoms in a multicenter

setting across numerous PET/CT systems to establish generally accepted RC values.

8. FUTURE DIRECTIONS IN PET IMAGING

We recognize that PET/CT technology is continuously evolving, particularly with the ongoing improvements in digital PET systems, machine learning-based image reconstruction, and other innovations. To address this, we suggest that the framework for calculating RCs and correcting PVE, as outlined in our study, can be adapted to accommodate future technological advancements. We believe that the core methodology, particularly the use of anthropomorphic phantoms, remains robust and adaptable to emerging systems. To broaden the applicability of our findings, we encourage further validation studies across an even wider array of PET/CT systems, including the newest generation of scanners. By extending our methodology to newer systems or integrating artificial intelligence-driven reconstruction techniques, the generalizability of the PVE correction approach can be further solidified.

REFERENCES

1. Alavi, A., T. J. Werner, P. F. Høilund-Carlsen, and H. Zaidi, "Correction for partial volume effect is a must, not a luxury, to fully exploit the potential of quantitative pet imaging in clinical oncology," *Molecular Imaging and Biology*, Vol. 20, pp. 1–3, 2018.

2. Krempser, A. R., R. M. Ichinose, A. M. Miranda de Sá, S. M. Velasques de Oliveira, and M. P. Carneiro, "Recovery coefficients determination for partial volume effect correction in oncological pet/ct images considering the effect of activity outside the field of view," *Annals of Nuclear Medicine*, Vol. 27, pp. 924–930, 2013.

3. Lu, S., P. Zhang, C. Li, J. Sun, W. Liu, and P. Zhang, "A nim pet/ct phantom for evaluating the pet image quality of micro-lesions and the performance parameters of ct," *BMC Medical Imaging*, Vol. 21, pp. 1–13, 2021.

4. Gallivanone, F., C. Canevari, L. Gianolli, C. Salvatore, P. Della Rosa, M. Gilardi, and I. Castiglioni, "A partial volume effect correction tailored for 18f-fdg-pet oncological studies," *BioMed Research International*, Vol. 2013, no. 1, p. 780458, 2013.

5. Adler, S., J. Seidel, P. Choyke, M. V. Knopp, K. Binzel, J. Zhang, C. Barker, S. Conant, and R. Maass-Moreno, "Minimum lesion detectability as a measure of pet system performance," *EJNMMI Physics*, Vol. 4, pp. 1–14, 2017.

6. Kessler, R. M., J. R. Ellis Jr, and M. Eden, "Analysis of emission tomographic scan data: limitations imposed by resolution and background," 1984.

7. Bettinardi, V., I. Castiglioni, E. De Bernardi, and M. Gilardi, "Pet quantification: strategies for partial volume correction," *Clinical and Translational Imaging*, Vol. 2, pp. 199–218, 2014.

8. Krane, K. S., *Introductory Nuclear Physics*, John Wiley & Sons, 1991.

9. Karmaker, N., K. M. Maraz, F. Islam, M. M. Haque, M. Razzak, M. Mollah, M. Faruque, and R. A. Khan, "Fundamental characteristics and application of radiation," *GSC Advanced Research and Reviews*, Vol. 7, no. 1, pp. 064–072, 2021.

10. Tavernier, S., *Experimental techniques in nuclear and particle physics*, Springer Nature, 2010.

11. Lewandowski, T. A., J. K. Chandalia, and P. A. Valberg, "Ionizing radiation," *Hamilton & Hardy's Industrial Toxicology*, pp. 1055–1068, 2015.

12. Cherry, S. R., J. A. Sorenson, and M. E. Phelps, *Physics in Nuclear Medicine*, Saunders, 2013.

13. Workman Jr, R. B., and R. E. Coleman, "Fundamentals of pet and pet/ct imaging," in *PET/CT: Essentials for Clinical Practice*, pp. 1–22, Springer, 2006.

14. Krishnamurthy, G. T., and S. Krishnamurthy, *Nuclear Hepatology: a Textbook of Hepatobiliary Diseases*, Springer, 2000.

15. Gillies, R. J., I. Robey, and R. A. Gatenby, "Causes and consequences of increased glucose metabolism of cancers," *Journal of Nuclear Medicine*, Vol. 49, no. Suppl 2, pp. 24S–42S, 2008.

16. Hsu, P. P., and D. M. Sabatini, "Cancer cell metabolism: Warburg and beyond," *Cell*, Vol. 134, no. 5, pp. 703–707, 2008.

17. Altenberg, B., , and K. Greulich, "Genes of glycolysis are ubiquitously overexpressed in 24 cancer classes," *Genomics*, Vol. 84, no. 6, pp. 1014–1020, 2004.

18. Jacobson, M. S., R. A. Steichen, and P. J. Peller, "Pet radiochemistry and radiopharmacy," in *PET-CT and PET-MRI in Oncology: A Practical Guide*, pp. 19–30, Springer, 2012.

19. Elsinga, P. H., "Present and future of pet-radiopharmaceuticals," *Nuclear Medicine Review*, Vol. 15, no. C, pp. 13–16, 2012.

20. Martin, C. J., "The application of effective dose to medical exposures," *Radiation Protection Dosimetry*, Vol. 128, no. 1, pp. 1–4, 2008.

21. Bernier, D., J. K. Langan, and L. D. Wells, "Nuclear medicine technology and techniques," *Nuclear Medicine Technology and Techniques*, 1981.

22. Bayhan, H., "Pozitron emisyon tomografi (pet) tarihçesi.," *Bulletin of Thoracic Surgery/Toraks Cerrahisi Bülteni*, Vol. 6, no. 2, 2015.

23. Lin, E., and A. Alavi, *Pet and Pet/CT.*, Thieme Medical Publishers, 2009.

24. Bushberg, J., J. Seibert, E. Leidholdt Jr, and J. Boone, "The essential physics of medical imaging. 2002," *European Journal of Nuclear Medical Molecular Imaging*, Vol. 30, p. 1713, 2003.

25. Rezvani, S., P. Ghafarian, M. B. Karam, and M. Ay, "Role of lesion-to-background activity ratio and background activity in optimization of reconstruction protocols for fdg pet/ct images of overweight patients: A phantom study," *Iranian Journal of Radiology*, Vol. 20, no. 1, 2023.

26. Koopman, D., J. A. van Dalen, H. Stevens, C. H. Slump, S. Knollema, and P. L. Jager, "Performance of digital pet compared with high-resolution conventional pet in patients with cancer," *Journal of Nuclear Medicine*, Vol. 61, no. 10, pp. 1448–1454, 2020.

27. Salvadori, J., F. Odille, A. Verger, P. Olivier, G. Karcher, P.-Y. Marie, and L. Imbert, "Head-to-head comparison between digital and analog pet of human and phantom images when optimized for maximizing the signal-to-noise ratio from small lesions," *EJNMMI Physics*, Vol. 7, pp. 1–14, 2020.

28. Driscoll, B., T. Shek, D. Vines, A. Sun, D. Jaffray, and I. Yeung, "Phantom validation of a conservation of activity-based partial volume correction method for arterial input function in dynamic pet imaging," *Tomography*, Vol. 8, no. 2, pp. 842–857, 2022.

29. Alavi, A., T. J. Werner, P. F. Høilund-Carlsen, and H. Zaidi, "Correction for partial volume effect is a must, not a luxury, to fully exploit the potential of quantitative pet imaging in clinical oncology," *Molecular Imaging and Biology*, Vol. 20, pp. 1–3, 2018.

30. Meechai, T., S. Tepmongkol, and C. Pluempitiwiriyawej, "Partial-volume effect correction in positron emission tomography brain scan image using super-resolution image reconstruction," *The British Journal of Radiology*, Vol. 88, no. 1046, p. 20140119, 2015.

31. Srinivas, S. M., T. Dhurairaj, S. Basu, G. Bural, S. Surti, and A. Alavi, "A recovery coefficient method for partial volume correction of pet images," *Annals of Nuclear Medicine*, Vol. 23, pp. 341–348, 2009.

32. Rousset, O., A. Rahmim, A. Alavi, and H. Zaidi, "Partial volume correction strategies in pet," *PET Clinics*, Vol. 2, no. 2, pp. 235–249, 2007.

33. Oliveira, C. M., T. A. d. Silva, I. F. Vieira, F. R. Lima, J. W. Vieira, L. V. d. Sa, *et al.*, "Characterization of a pet-nema/iec body phantom for quality control tests of pet/ct equipment," *ETDEWEB Conference OSTI ID 21578612*, 2011.

34. Paliwal, B., and D. Tewatia, "Advances in radiation therapy dosimetry," *Journal of Medical Physics*, Vol. 34, no. 3, pp. 108–116, 2009.

35. Thwaites, D., "Accuracy required and achievable in radiotherapy dosimetry: have modern technology and techniques changed our views?," in *Journal of Physics: Conference Series*, Vol. 444, p. 012006, IOP Publishing, 2013.

36. DOSE, W. B., O. DOSE, and T. Radiation, "Atom® dosimetry phantoms," 2013.

37. Fedrigo, R., D. J. Kadrmas, P. E. Edem, L. Fougner, I. S. Klyuzhin, M. P. Petric, F. Bénard, A. Rahmim, and C. Uribe, "Quantitative evaluation of psma pet imaging using a realistic anthropomorphic phantom and shell-less radioactive epoxy lesions," *EJNMMI Physics*, Vol. 9, no. 1, p. 2, 2022.

38. National Electrical Manufacturers Association, *Performance Measurements of Positron Emission Tomographs (NEMA Standards Publication NU 2-2018)*, Rosslyn, VA: National Electrical Manufacturers Association, 2018. NEMA Standards Publication NU 2-2018.

39. Kovan, B., *İnternal Radyonüklid Tedavisinde Organ Doz Hesaplama Parametrelerinin Optimizasyonu.* Doctoral dissertation, İstanbul Üniversitesi, Fen Bilimleri Enstitüsü, İstanbul, Türkiye, 2021.

40. Lennie, E., C. Tsoumpas, and S. Sourbron, "Multimodal phantoms for clinical pet/mri. ejnmmi physics. 2021; 8 (62)."

41. Matheoud, R., C. Secco, P. Della Monica, L. Leva, G. Sacchetti, E. Inglese, and M. Brambilla, "The effect of activity outside the field of view on image quality for a 3d lso-based whole body pet/ct scanner," *Physics in Medicine & Biology*, Vol. 54, no. 19, p. 5861, 2009.

42. Hsu, D. F., E. Ilan, W. T. Peterson, J. Uribe, M. Lubberink, and C. S. Levin, "Studies of a next-generation silicon-photomultiplier–based time-of-flight pet/ct system," *Journal of Nuclear Medicine*, Vol. 58, no. 9, pp. 1511–1518, 2017.